

Single- and Dual-Doppler Analysis of a Tornadic Vortex and Surrounding Storm-Scale Flow in the Crowell, Texas, Supercell of 30 April 2000

JAMES MARQUIS AND YVETTE RICHARDSON

The Pennsylvania State University, University Park, Pennsylvania

JOSHUA WURMAN

Center for Severe Weather Research, Boulder, Colorado

PAUL MARKOWSKI

The Pennsylvania State University, University Park, Pennsylvania

(Manuscript received 30 October 2007, in final form 7 May 2008)

ABSTRACT

Fine-resolution single- and dual-Doppler data were collected in the tornadic region of a supercell storm intercepted by two Doppler-on-Wheels radars on 30 April 2000 near Crowell, Texas. Eleven dual-Doppler analyses characterize the 2D and 3D near-surface wind fields associated with a tornado during a 13-min period. An interesting evolution of the low-level rotation is observed. Initially concentric “tornado” (~500 m wide) and “tornado–cyclone” (~2 km wide) radar velocity couplets make a transition into a solitary intermediate-sized (~750 m wide) circulation that widens and makes a further transition into a two-celled multiple-vortex structure with an asymmetric distribution of vertical vorticity. The asymmetry and eventual disruption of the multiple-vortex structure may have been partially controlled by locally strong outflow winds that affect the convergence fields in its vicinity. A smaller (~500 m wide) tornado embedded in a broad area of rotation is subsequently observed. The dual-Doppler wind fields are also used to characterize aspects of the storm-scale flow. Locally surging outflow winds result in a double rear-flank gust front structure. The tornado and tornado–cyclone are completely surrounded by outflow at all observation times and air parcels traced within the inflow to the storm rise along the gust front rather than enter the tornado near the ground.

1. Introduction

Many numerical modeling, laboratory, observational, and theoretical studies have been employed in the past to develop conceptual models of tornado structure and behavior. For example, tornado vortex structure has been consistently produced using laboratory and numerically simulated fluid chambers (e.g., Ward 1972; Dessens 1972; Davies-Jones 1973; Rotunno 1984; Lewellen et al. 1997, 2000). Such studies show that one-celled vortices are obtained under certain conditions while two-celled multiple-vortex structures, in which small secondary vortices forming via cylindrical shear-ing instability orbit the larger-scale circulation, form

under other conditions that may or may not include vortex breakdown (Trapp 2000). These vortex models are highly simplified and finescale observations to validate them are rare.

Some numerical modeling studies have focused on understanding the evolution of the overall storm-scale structure in order to assess its influence on the formation and maintenance of a tornado (e.g., Klemp and Rotunno 1983; Wicker and Wilhelmson 1995; Grasso and Cotton 1995; Trapp and Fiedler 1995; Straka et al. 2007). Collectively, such studies have shown that the tornadic area of the storm is typically located where storm-scale updrafts and downdrafts meet, updrafts at times show distinct vorticity maxima within a ring of vorticity prior to tornadogenesis, and air parcels surrounding the tornado originate both from the ambient environment (with subsequent flow through a region of evaporatively chilled air and downdraft along the forward flank) and from the area behind (in a storm-

Corresponding author address: James Marquis, The Pennsylvania State University, 503 Walker Building, University Park, PA 16802.

E-mail: jmarquis@met.psu.edu

relative sense) the rear-flank gust front. The rear-flank downdraft has been implicated as important to the tornadogenesis process, but its exact role in either genesis or subsequent maintenance is subject to debate. Understanding this role has been hampered by the inability of numerical models to produce realistic outflow (Markowski 2002) and by the paucity of finescale observations of the 3D structure in this region of the storm. Limited surface observations (Lee et al. 2004; Finley and Lee 2004) have suggested complex structure in the form of multiple surges within the rear-flank downdraft region, but the influence of these surges on developing or existing tornadoes is unknown.

To verify conceptual models regarding tornado structure and dynamics, many attempts have been made to collect kinematic and thermodynamic data in and surrounding them. Perhaps the most successful attempts to observe kinematic traits of tornadoes involve the use of Doppler radar. Several studies have described various kinematic aspects of tornadoes using single-Doppler radar data, such as their finescale vortex structure (e.g., Wurman et al. 1996, 1997; Bluestein and Pazmany 2000; Wurman and Gill 2000; Wurman 2002; Bluestein et al. 2003, 2004; Alexander and Wurman 2005), estimations of their angular momentum budgets and axisymmetric flow (e.g., Lee and Wurman 2005; Rasmussen and Straka 2007), their near-surface peak wind intensity and damage potential (Wurman and Alexander 2005; Wurman et al. 2007c), and debris/hydrometeor centrifuging (Dowell et al. 2005). Some single-Doppler data indicate concentric tornado-scale vortices embedded within the mesocyclone (e.g., Wurman and Alexander 2004). The dynamics governing the interaction of these scales is not well known and is the subject of recent research regarding tornado intensification at low levels (e.g., Rasmussen and Straka 2007; Lewellen and Lewellen 2007a,b).

A more complete representation of the 3D wind field surrounding a tornado can be made with radar data using dual-Doppler syntheses. Dual-Doppler data collected in a few tornadic supercells prior to and during the Verification of the Origins of Rotation in Tornadoes Experiment (VORTEX; Rasmussen et al. 1994) have advanced our understanding of storm-scale flow surrounding tornadoes and have provided new hypotheses regarding tornado formation and maintenance (Brandes 1977, 1978, 1981, 1984; Dowell and Bluestein 1997; Wakimoto and Liu 1998; Dowell and Bluestein 2002). However, the spatial and temporal resolution available to these studies precludes the adequate observation of the 3D wind fields associated with features of a spatial scale less than a few kilometers. Additionally, because there are only a few dual-Doppler

datasets available that document the wind field in a supercell during the lifetime of a tornado, this small sample of cases must be supplemented to address the consistency of findings among different storms.

Since VORTEX, the Doppler-on-Wheels (DOW; Wurman et al. 1997) radars have collected finescale resolution data in close proximity to many tornadoes. Some of the storms were observed with two DOW radars simultaneously, providing the highest temporal (50–90 s) and spatial (100–300 m) resolution dual-Doppler wind analyses surrounding tornadoes ever achieved in the lowest few kilometers of a storm. The first DOW cases for which dual-Doppler data were available (Richardson et al. 2001; Dowell et al. 2002; Wurman et al. 2007a,b) show the evolution of near-surface rotation and values of certain terms in the vertical vorticity equation, such as stretching and tilting. The present study uses high-resolution single- and dual-Doppler radar data collected in a tornadic supercell storm intercepted by two DOWs near Crowell, Texas, on 30 April 2000. These data allow us to verify some past numerical and conceptual models of the low-level evolution of small-scale features and to relate the tornado to the storm-scale airflow. The analysis of this storm is part of a broader study assessing aspects of tornado maintenance using similar DOW data collected in several supercells. Section 2 describes the collection of the radar data for this case and the dual-Doppler methodology. Single-Doppler observations of the tornadic circulations are described in section 3, followed by dual-Doppler observations in section 4. Section 5 puts these dual- and single-Doppler data in the context of past studies, and section 6 highlights some outstanding questions that might be valuable to address in future studies. An appendix is provided to address the sensitivities of the analyses presented herein to certain aspects of the wind synthesis method.

2. Method

The Doppler radar data that are the focus of this study were collected in the tornadic region of the Crowell supercell between 2100 and 2130 UTC 30 April 2000. DOW2 was stationary and collected data from 2100 to 2102 UTC (at antenna elevation angles of 2.0°, 3.0°, and 4.0°, intersecting the tornado between approximately 450 m and 1.3 km AGL) before leveling the truck. When leveled, DOW2 collected data from 2104 to 2119 UTC and from 2122 to 2129 UTC at elevation angles of 0.5°, 1.5°, 2.0°, 2.5°, 3.5°, 4.5°, 6.5°, 10.4°, and 13.0°; intersecting the tornado between approximately 50 m and 2 km AGL. DOW3 collected level data from 2100 to 2119 UTC. During the first part

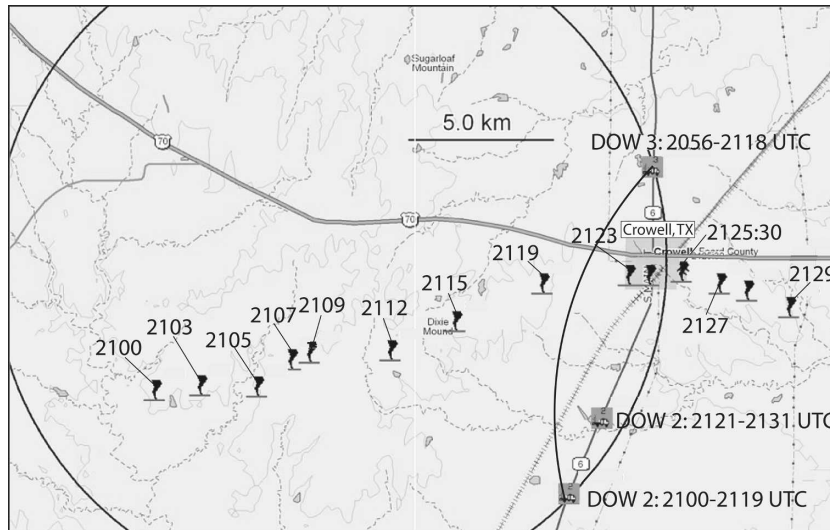


FIG. 1. Dual-Doppler deployment for the Crowell, TX, intercept. The dual-Doppler lobe and baseline region are indicated with black lines. Radar-determined tornado position is indicated at several times (UTC).

of the deployment (from 2100 to 2109 UTC), DOW3 performed very fine temporal resolution (~ 5 – 10 s) low-level (0.5° antenna elevation angle) scans, allowing us to follow the evolution of the near-surface ($z \leq 150$ m) flow surrounding the tornado. Later (from 2109 to 2118 UTC), DOW3 collected 3D volumes of data at antenna elevation angles of 0.5° , 2.0° , 3.5° , 5.0° , 6.5° , 8.0° , 9.5° , 11° , 12.5° , 14.0° , and 15.5° ; intersecting the tornado between approximately 75 m and 2 km AGL. Data collection began when the tornado was approximately 20 km WSW of the town of Crowell (Fig. 1). On average, the tornado was moving to the east-northeast at approximately 12 m s^{-1} during the observation period.

To facilitate analysis of data on a common grid for the dual-Doppler wind synthesis, the mobile radar data (collected in a truck-relative frame) are rotated to an earth-relative framework by aligning low-level ground clutter echoes with known locations of power poles, towers, and houses. The precise locations of these targets are determined from high-resolution aerial photographs. This technique yields a presumed alignment precision of about 0.2° ; perturbations to the assumed alignment of $\leq 0.2^\circ$ also yield an overlap of clutter echoes with photographed structures. The motion of the tornado over the time needed to collect a volume of radar data is accounted for by correcting the position of each datum to its most likely location at the central volume time. This prevents an artificial tilt with height of storm features due to their motion between consecutive radar sweeps. When a dual-Doppler solution is possible, the single-Doppler radar data (edited to remove ground clutter and aliased velocities) are objec-

tively analyzed to a Cartesian grid with an isotropic Barnes weighting function (Barnes 1964). The objective analysis parameters are chosen based on the coarsest azimuthal data resolution ($\delta = R\theta$, where R is the range from radar and θ , the beamwidth of the radar, is 0.93° for the DOWs) observed in the desired domain (Trapp and Doswell 2000). The smoothing parameter, $\kappa = (1.33\delta)^2$ (Pauley and Wu 1990), and the Cartesian grid spacing, $\Delta = \delta/2.5$ (Koch et al. 1983). The Cartesian grid dimensions are $20 \text{ km} \times 25 \text{ km} \times 3 \text{ km}$. A cutoff radius, $R_c = 3\delta$, is used to decrease computational time of the objective analysis (Pauley and Wu 1990). One set of objective analyses that is designed to capture overall storm structure and evolution is produced using $\kappa = 0.187 \text{ km}^2$, $\Delta = 150 \text{ m}$, and $R_c = 975 \text{ m}$ (hereafter referred to as smoothing set 1). A second set of analyses that is designed to retain details of the flow in close proximity to the tornado is produced using $\kappa = 0.047 \text{ km}^2$, $\Delta = 75 \text{ m}$, and $R_c = 487 \text{ m}$ (hereafter referred to as smoothing set 2).

The 3D wind field is synthesized by an upward integration of the anelastic mass continuity equation with the lower boundary condition of $w = 0$ at $z = 0$. An iterative technique was used to adjust the u , v , and w fields until the change in the density-weighted w between iterations is less than $0.01 \text{ kg m}^{-2} \text{ s}^{-1}$. Because the lowest elevation angle scanned by the DOWs is 0.5° , a downward extrapolation of wind data is necessary in order to apply the lower boundary condition. This extrapolation is performed by setting the missing low-level u and v wind components equal to those at the next level at which both radars collect data. For most

analyses presented herein, the lowest level for which both radars provide data is one grid point above the ground; therefore, the necessary extrapolation is minimal. Corrections for the centrifuging and falling of debris and hydrometeors are not performed because of power attenuation along beams in the heavy precipitation, an uncalibrated DOW reflectivity factor, and an unknown scatterer type. Fall speed errors are assumed to be small because of the relatively small antenna elevation angles used (i.e., $<15.5^\circ$).

Eleven dual-Doppler analyses are available from approximately 2104 to 2117 UTC at time intervals of 60–90 s. Six dual-Doppler analyses available from 2104 to 2110 UTC are on 2D, nearly horizontal planes near the ground due to the DOW3 scanning strategy. Five dual-Doppler analyses available between approximately 2110 and 2117 UTC cover 3D volumes surrounding the tornadic area of the storm from the ground up to $z = 1.5\text{--}3$ km AGL. The antenna elevation angle lists were chosen such that 3D volumes of data could be rapidly collected at low levels in the storm; therefore, radar data are not available at mid- through upper levels of the storm. The single-Doppler data from each radar that are combined in the dual-Doppler syntheses are collected at similar heights AGL between 10 and 20 s apart for the 3D volumes and typically <5 s apart for the 2D analyses (except in two analyses when the time differences are 10 and 25 s). In the 2D wind syntheses, individual 0.5° DOW3 sweeps are combined with DOW2 data that are interpolated between the 0.5° and 1.5° sweeps to produce horizontal winds analyzed within 15–30 m of the DOW3 observed heights AGL at the tornado.

3. Single-Doppler data

The DOW-observed peak intensity of the Crowell tornado is relatively weak (peak near-surface tangential wind speed ≤ 45 m s $^{-1}$) in comparison with some other DOW-observed tornadoes (e.g., ~ 100 m s $^{-1}$; Alexander and Wurman 2005). Photographic images of a condensation funnel are not available due to the high-precipitation nature of this storm, and no significant damage was caused by this tornado, as it occurred over open land. Nevertheless, an interesting evolution of tornado vortex structure is observed by the DOWs over a 30-min period: two concentric circulations transition into one intermediate-sized circulation that exhibits a multiple-vortex structure for a brief time before returning to a concentric circulation pair and ultimately transitioning into a single vortex before tornado demise. This complicated evolution of tornado structure is now described using single-Doppler velocity observations.

Select images from a 30-min sequence of continuous

DOW-relative Doppler velocity observations (V_r ; i.e., vortex tangential velocity at a constant radar range corresponding to the center of rotation) focused on the tornado, and Weather Surveillance Radar-1988 Doppler (WSR-88D) reflectivity and velocity data [from Lubbock, Texas (KLBB)] showing the overall storm structure at 2107 UTC are shown in Fig. 2. The mid- and low-level mesocyclone (Fig. 2l) is well defined even when viewed at great range with KLBB and is surrounded by >30 dBZ, indicating a high-precipitation storm type. Near the surface, two concentric inbound–outbound V_r couplets are observed at the start of DOW observations (Fig. 2a), one with a core diameter (distance between peak inbound and outbound V_r maxima), $D \approx 400$ m, and another with $D \approx 2$ km. These couplets have similar azimuthal wind shear, defined here as the difference between peak inbound and outbound V_r maxima, $\Delta V_r \approx 62$ m s $^{-1}$. The azimuthal beamwidth of DOW3 probably does not allow the data to completely resolve the smaller scale, but concurrent data collected by DOW2 have higher spatial resolution and also show a distinct concentric pair present at $z = 400$ m AGL up to at least $z = 1.3$ km AGL (Figs. 3a–c). The smaller scale of rotation is nearly centered in the larger-scale V_r couplet until about 2102 UTC (Fig. 2b), when the tracking of the outer circulation becomes difficult. By 2103 UTC (Fig. 2c), only one circulation is distinguishable at low levels, with $\Delta V_r \approx 70$ m s $^{-1}$ and $D \approx 730$ m. However, concentric scales are still observed above the ground (Figs. 3e,f). Between 2103 and 2109 UTC (Figs. 2c–e), the V_r couplet widens but has a generally steady ΔV_r . From approximately 2107:11 to 2108:56 UTC (e.g., Fig. 2e), there is evidence of smaller areas of rotation with spatial scales of a few hundred meters surrounding the core of the larger V_r couplet, suggesting a multiple-vortex signature (e.g., Wurman 2002). Between approximately 2108 and 2109 UTC, the westernmost of these secondary vortices becomes prominent and slants eastward with height more than the approximately 1.8-km-wide V_r couplet such that the two are nearly concentric aloft (Figs. 3g–i). Distinct secondary vortices are no longer easily discerned by 2110 UTC (Fig. 2f) using single-Doppler data, and the majority of the wind shear across the approximately 2-km-wide V_r couplet in which they were embedded becomes concentrated on its western side.

DOW3 begins collecting full 3D volumes of data at approximately 2110 UTC, changing from 5–10 s to ~ 90 -s temporal resolution at low levels; therefore, the precise tracking of tornado-scale features is more difficult than in prior minutes. At 2111:44 UTC (Fig. 2g), when the first 0.5° elevation angle sweep is available after the change in temporal resolution, the most

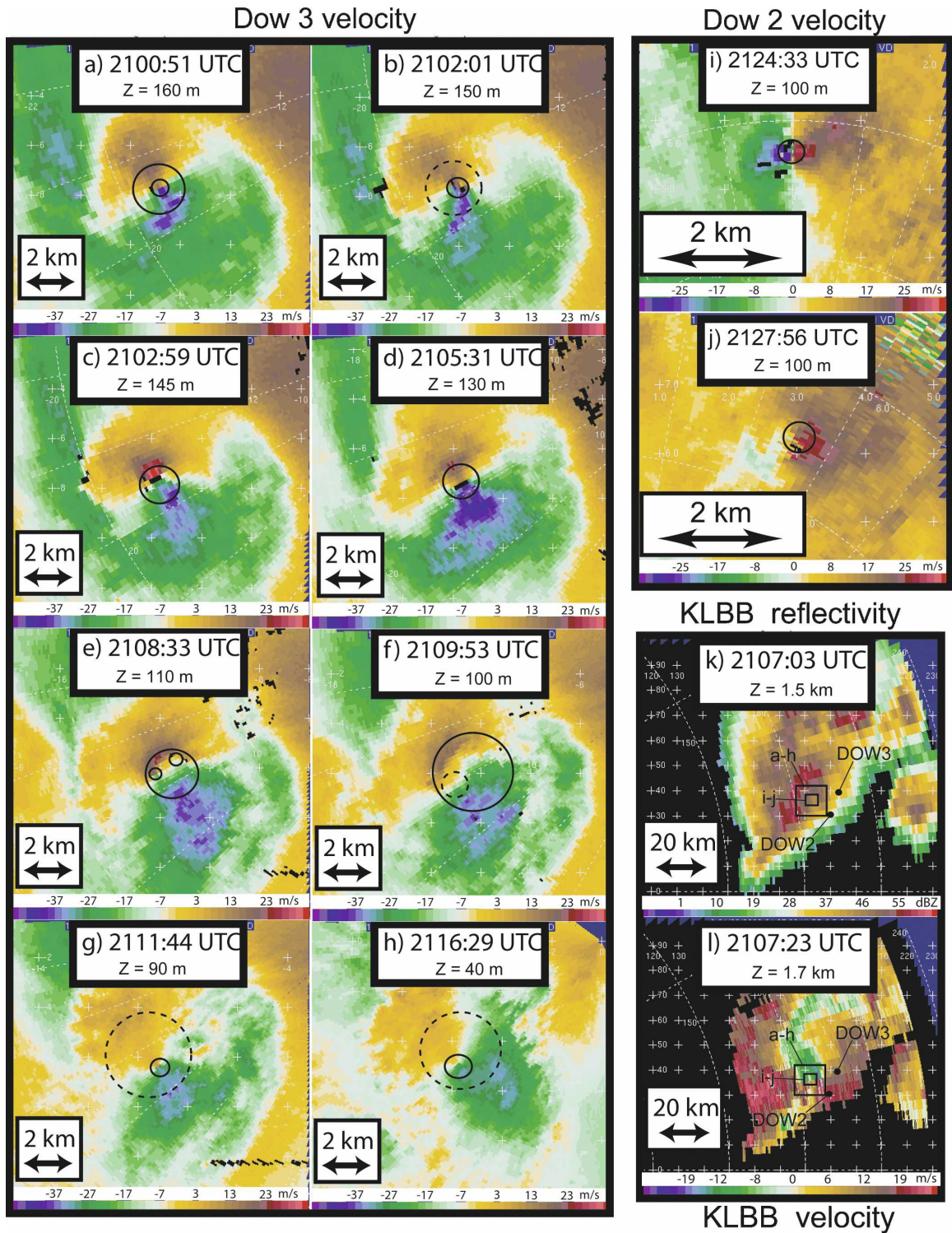


FIG. 2. Single-Doppler radial velocity data collected between 2100:51 and 2127:56 UTC from the 0.5° elevation sweeps of (a)–(h) DOW3 and (i), (j) DOW2. Prominent submesoscale velocity couplets are indicated in (a)–(j) with circles. Difficulty in the subjective identification of prominent velocity couplets is indicated with dashed circles. (k), (l) Velocity and reflectivity data collected by the WSR-88D in Lubbock, TX, (KLBB) at approximately 2107 UTC. The approximate locations of the (a)–(h) DOW3 and (i), (j) DOW2 data are illustrated relative to the overall storm with boxes in (k) and (l), and the approximate deployment locations of each of the DOWs are shown with dots. The approximate heights at which the sweeps intersect the tornado are indicated. Range rings and spokes are provided to indicate radar location.

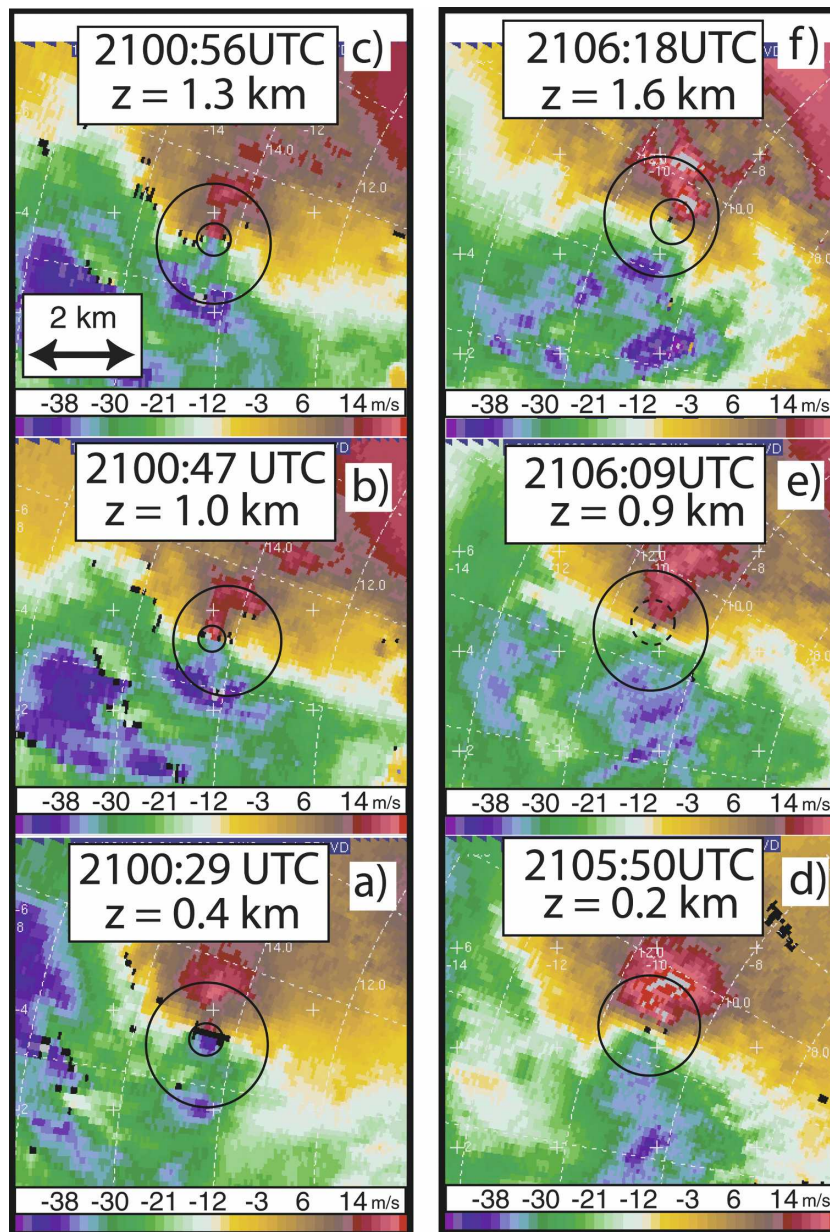


FIG. 3. Single-Doppler radial velocity data at three elevation angles from four 3D volume scans collected by DOW2. The approximate height and time at which each sweep intersects the tornado are indicated. Prominent velocity couplets are indicated with circles. Difficulty in the subjective identification of prominent velocity couplets is indicated with dashed circles.

prominent features observed include a small (~ 400 m wide) V_r couplet located within a broader (~ 3 km wide) area of rotation, the latter presumably being the larger-scale V_r couplet observed to broaden rapidly in the prior 2 min. The 3-km-wide circulation appears to narrow after about 2112 UTC, but the smaller scale of rotation remains approximately 600 m wide after 2113 UTC (although, it briefly reaches $D = 900$ m at 2117:40

UTC). Values of ΔV_r (≈ 35 m s^{-1}) are their weakest for both scales of rotation at the end of DOW3 observations. A tornado is observed by DOW2 to reach $\Delta V_r \approx 65$ m s^{-1} at ~ 2124 UTC (Fig. 2i); however, because of a 2-min data outage starting at 2119 UTC, it is unclear if this tornado is new or is a strengthening of the 600-m-wide tornado observed between 2112 and 2119 UTC. This tornado is observed to dissipate at approximately

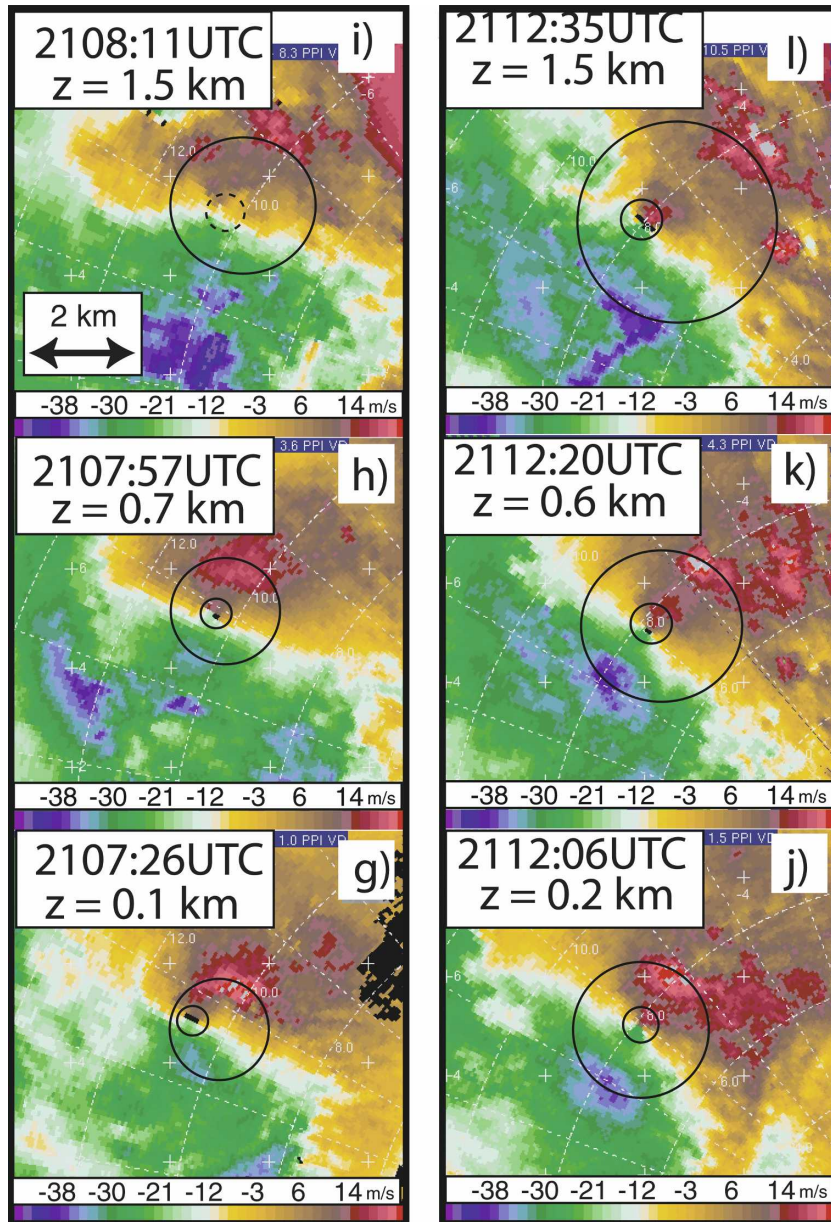


FIG. 3. (Continued)

2129 UTC (shortly after Fig. 2j). Only one scale of rotation is observed in the 3D data between 2120 and 2129 UTC, contrary to the concentric scales of rotation observed at prior times.

The evolution of the scales of low-level rotation between the times shown in Figs. 2a–h is illustrated in a Hovmöller diagram of the peak DOW3-observed V_r values (with the average motion of the tornado toward the radar subtracted) as a function of time and azimuthal distance across the tornado, and estimated values of circulation about a vertical axis ($\Gamma \approx \pi \Delta V_r D/2$) for the prominent V_r shear signatures (Fig. 4). The mag-

nitude of the tangential velocity of each V_r couplet generally is symmetric about $x = 0$ except between 2102 and 2103 UTC, when the outbound values are considerably stronger than the inbound values. The exact reasons for this asymmetry are not clear. Also occurring around this time is a transition of two concentric scales of rotation into one at the ground. It is possible that a partial contraction of angular momentum associated with the original 2-km-wide circulation occurs between 2102:00 and 2102:35 UTC; peak values of V_r for the outer couplet become nearly indiscernible while peak values of V_r closer to $x = 0$ increase (Fig. 4a). Gusting

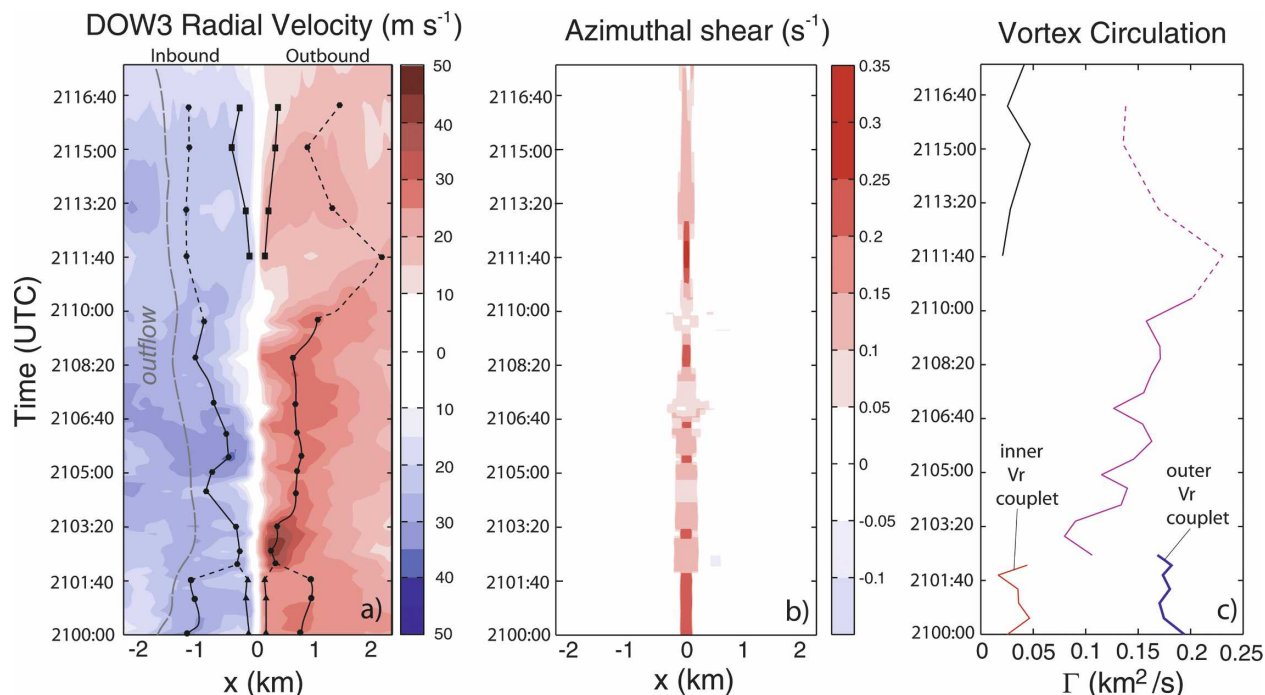


FIG. 4. Hovmöller diagram of the maximum magnitude of (a) DOW3-observed radial velocity and (b) azimuthal shear as a function of time and azimuthal distance across the tornado ($x = \pm 2$ km) using the available 0.5° elevation angle sweeps. (c) An estimation of circulation, Γ , for each of the prominent V_r couplets [whose subjectively identified V_r minima and maxima are traced with dots and thin lines in (a)] is shown as a function of time. In (a), inbound velocities (toward the radar) are shaded in blue, outbound velocities (away from the radar) are shaded in red, and the average motion of the tornado toward the radar (~ 12 m s $^{-1}$) is removed. Data are aligned such that the zone of maximum shear across the V_r couplets (an estimation of the center of the tornado) is centered at $x = 0$ at each time. The narrowing of the shear measurements in time in (b) is due to the increasing spatial resolution of data collected by the radar as the tornado approaches it. Fine dashed lines in the left and right panels indicate uncertainty in the subjective identification of the V_r minima and maxima and circulation associated with the prominent V_r couplets. The gray dashed line on the left side of (a) identifies gusty storm outflow winds south of the tornado.

outflow air south of the tornado (subjectively identified in Fig. 4a as transient inbound V_r maxima located south of the tornado by at least one width of the low radar reflectivity eye associated with the tornado) sometimes makes the identification of the inbound maximum of the V_r couplets more difficult than the outbound side. For example, a maximum in outbound V_r is seen between $x = 0$ and 1.0 km (except when the prominent circulation is rapidly widening between 2108 and 2111:30 UTC), while a similar maximum in inbound V_r is not as obvious.

4. Dual-Doppler observations

The continuous dual-Doppler data from 2104 to 2117 (e.g., Fig. 5) captures many features consistent with the supercell conceptual model at low levels (Lemon and Doswell 1979). The rear-flank gust front (evident as a line of convergence with a wind shift) encircles the area of strongest rotation at all observation times, indicating that the tornado is completely surrounded by outflow

air. A broader and generally more diffuse line of convergence extends to the northeast from a point where it intersects the rear-flank gust front about 4 km north of the vorticity maximum. This convergence line is consistent with a forward-flank gust front, but is located within heavy precipitation observed by the DOWs (thin contours in Fig. 5) on the forward-flank of the storm rather than leading it. However, it should be noted that beam attenuation is problematic for the DOWs on the western half of the observed domain because of the high-precipitation nature of the storm; therefore, the location of the forward-flank gust front relative to the area of heaviest precipitation is unclear. The position of the gust fronts (heavy solid lines in Fig. 5) relative to the vorticity maximum at the surface is nearly constant during the 13 min of dual-Doppler data. A broad area of near-surface divergence is found west through south of the vorticity maximum, consistent with a rear-flank downdraft. A small area of inflow to the analyzed portion of the storm is observed just east of the gust fronts. It is not clear how representative this air is to the me-

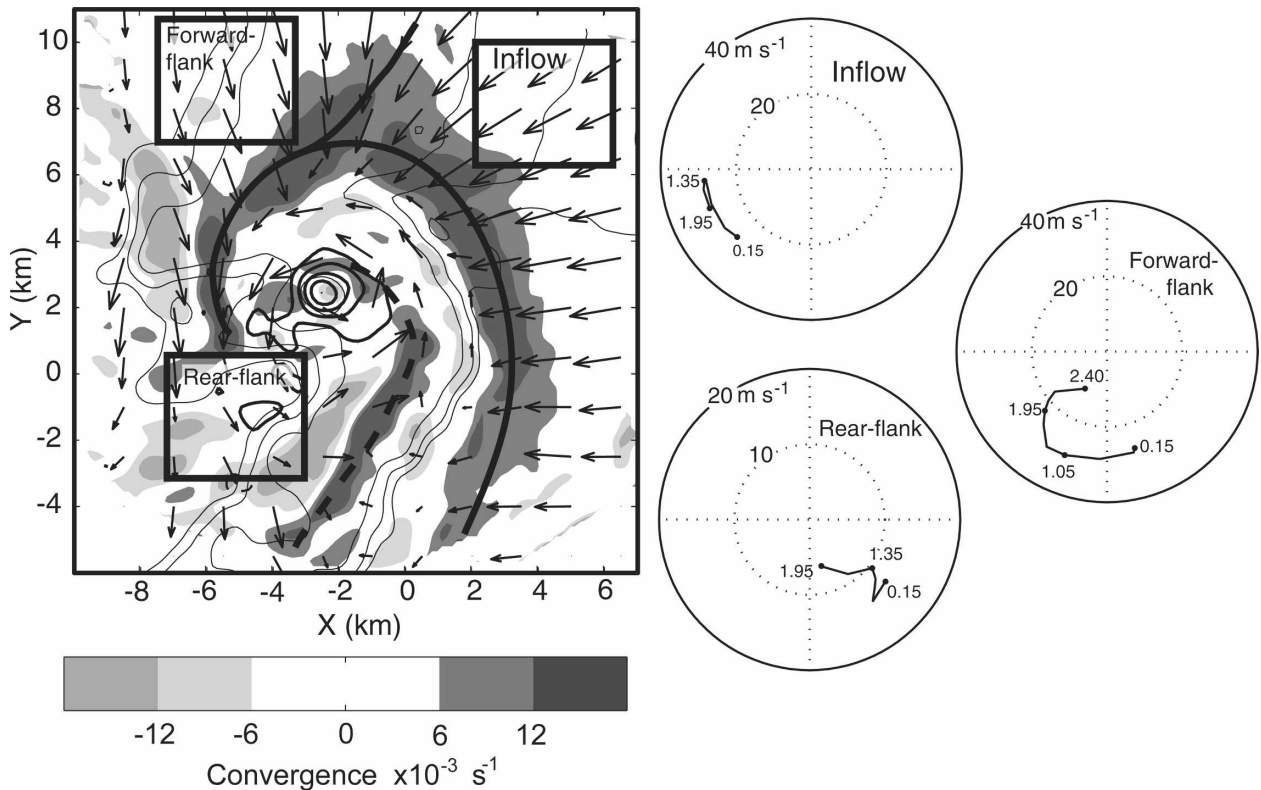


FIG. 5. (left) Horizontal plane of convergence (shaded), vertical vorticity (thick contours), DOW3 reflectivity (thin contours), and storm-relative wind (vectors) at $z = 150$ m AGL produced using smoothing set 1 at approximately 2107 UTC. The outermost contour of vertical vorticity is 0.02 s^{-1} , incremented by 0.025 s^{-1} . The outermost contour of DOW3 reflectivity is 20 dBZ, incremented by 5 dBZ. (right) Storm-relative hodographs produced by area-averaging the horizontal winds at each height in the three boxes that typify the observed portions of the inflow to the storm, the forward flank of the storm, and the rear flank of the storm at all analysis times. Primary forward-flank and rear-flank gust fronts are traced with heavy solid lines and a secondary rear-flank gust front is traced with a heavy dashed line. Heights (km AGL) are indicated at various points on the hodographs.

scale environment supporting the storm because most of the observed volume contains at least light precipitation ($\sim 20\text{--}35$ dBZ observed by KLBB in this region; Fig. 2k). However, this precipitation exists only a few kilometers ahead of the gust fronts.

At all analysis times, a shallow (below $z \approx 800$ m AGL) line of enhanced convergence (dashed line in Fig. 5) exists in the outflow air west of the rear-flank gust front and extends southward from a point near the surface vorticity maximum. Strong westerly outflow winds and divergence are found on the western side of this convergence swath at low levels, while much weaker winds and divergence are found on the eastern side. This convergence line resembles a secondary rear-flank gust front. The southern portion of this secondary gust front retains a nearly constant location relative to the vertical vorticity maximum until it surges to the east and northeast after 2112 UTC. This forward surge occurs in conjunction with strong divergence and southwesterly winds developing just east of the secondary

gust front at 2110 UTC. The formation process of the secondary gust front is not known; however, the fact that it is found just east of an area of strong near-ground divergence at all analysis times suggests that a localized downdraft (possibly a microburst and/or an occlusion downdraft) play a role in its formation and motion. Further thoughts regarding the secondary gust front are included in section 5.

An interesting evolution of the low-level vertical vorticity field is revealed using the dual-Doppler syntheses produced with smoothing set 2 (less smoothing). From 2104 to 2107 UTC (e.g., 2106:37 UTC; Figs. 6a,b), a generally symmetric vertical vorticity maximum ($\zeta_{\text{max}} = 0.19 \text{ s}^{-1}$) is located near a convergence–divergence dipole (and therefore a dipole in vertical vorticity stretching/compression). However, at 2107:35 UTC (Figs. 6c,d), a ring of vertical vorticity is found with strong divergence (vortex compression) located near the center, where vorticity has a local minimum (marked with an “N” in Fig. 6). The ring of vorticity is asymmetric

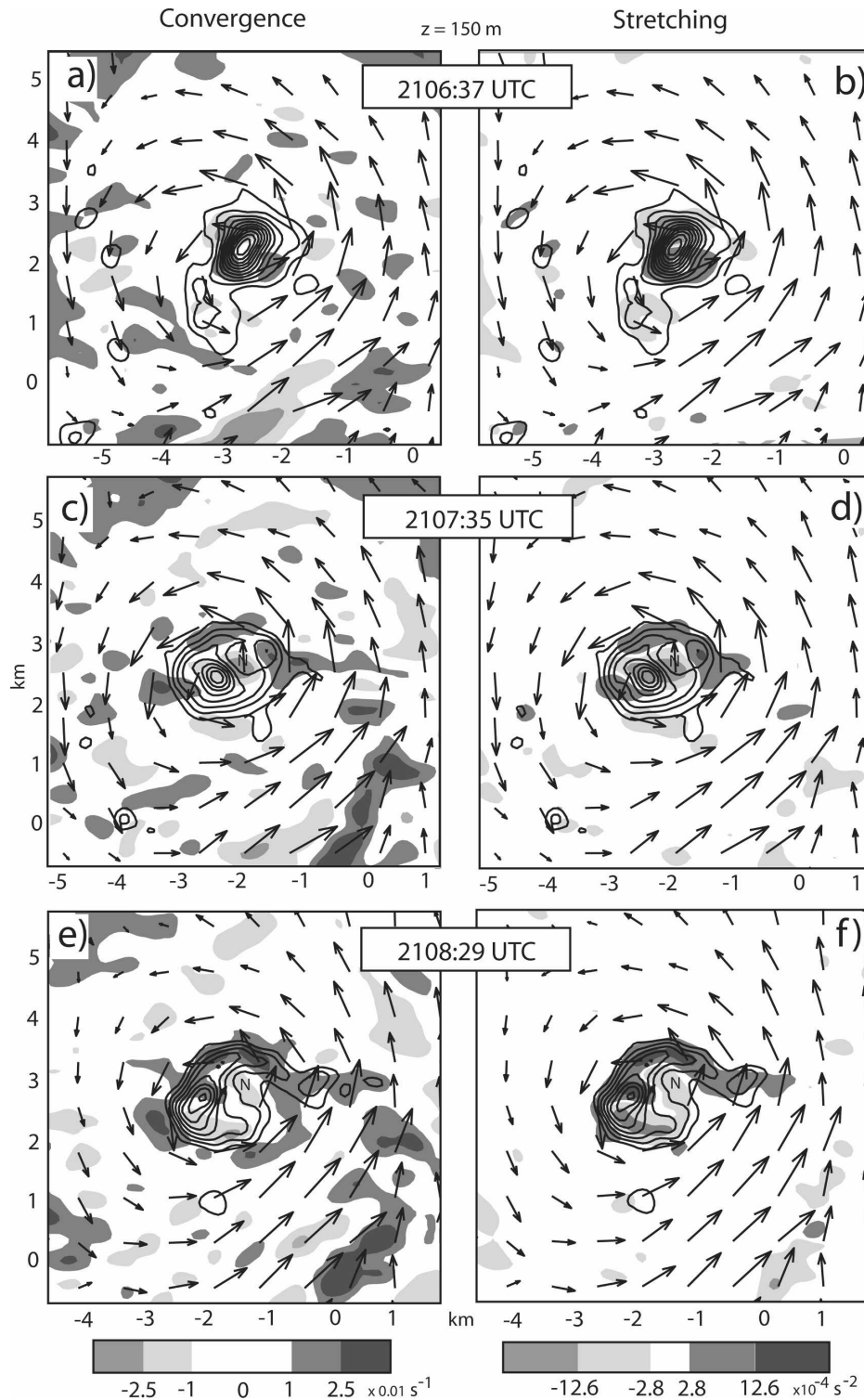


FIG. 6. Vertical vorticity (contoured), horizontal winds relative to the motion of the vorticity maximum at each analysis time (vectors), (left) convergence (shaded), and (right) stretching of vertical vorticity (shaded) at six different times at $z = 150\text{ m}$ AGL produced using smoothing set 2. The outermost contour of vertical vorticity is 0.03 s^{-1} , incremented by 0.015 s^{-1} . The “N” denotes the location of the vertical vorticity minimum described in the text.

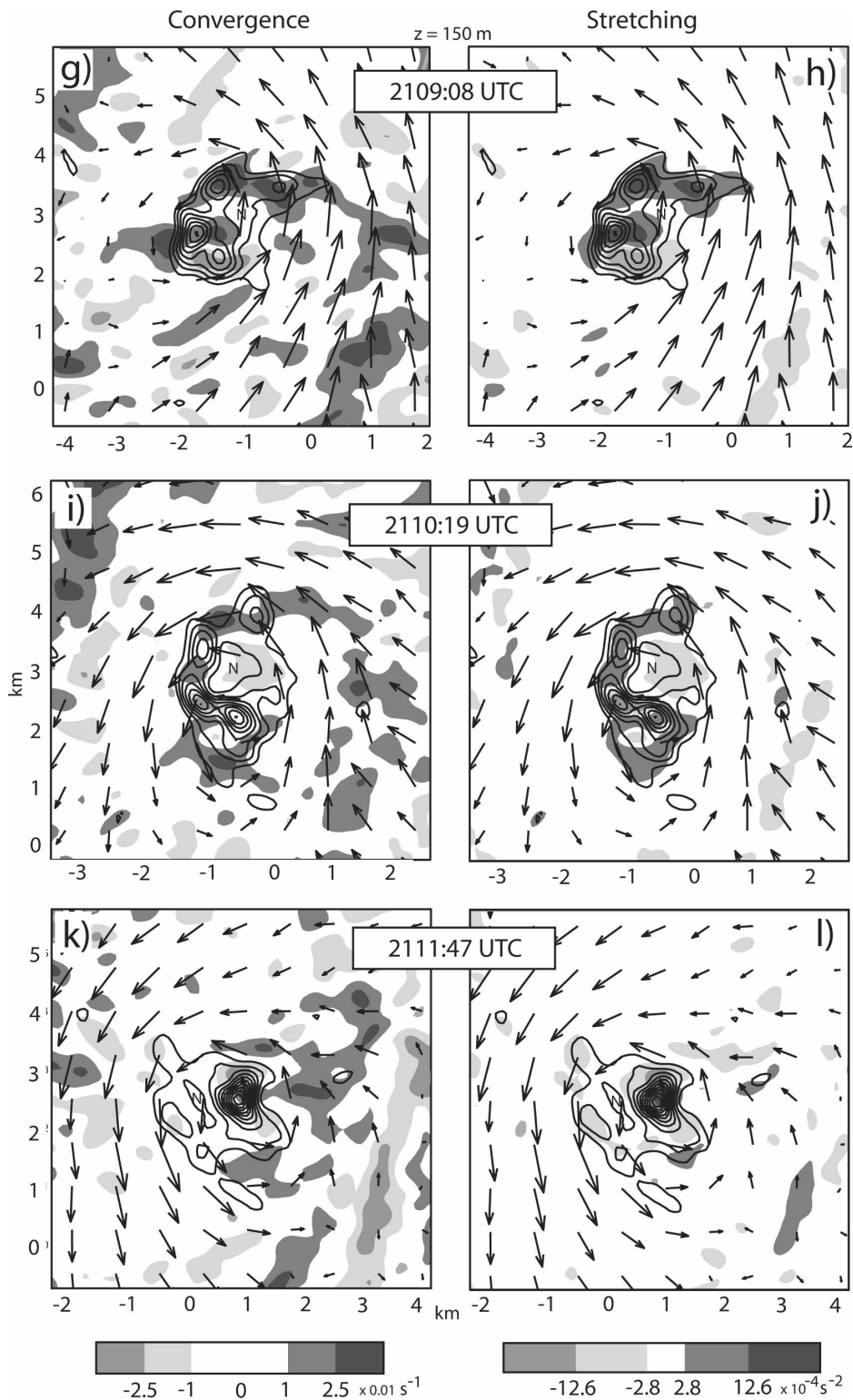


FIG. 6. (Continued)

about the center, with a maximum value on the southwest side. Over the next 3 min (Figs. 6e–j), the vorticity annulus widens and continues to be asymmetric with discrete vorticity maxima present on the western half of the ring, similar to the pattern observed in Wicker and Wilhelmson (1995). An isolated area of divergence remains close to the center of the vorticity ring (except at 2109:08 UTC, when this divergence is just south of the center of the ring), with an annulus of equally strong convergence surrounding it. The greatest vorticity in the ring is generally located close to the strong convergence annulus during this sequence; therefore, stretching is maximized around the periphery of the ring but minimized in its center. At 2111:47 UTC, a single vertical vorticity maximum is present (Figs. 6k,l) with an analyzed peak strength similar to that at 2106:35 UTC ($\zeta_{\max} = 0.18 \text{ s}^{-1}$), though weakening afterward until the end of dual-Doppler observations at 2117 UTC ($\zeta_{\max} = 0.15 \text{ s}^{-1}$). The exact details of the transition of the vortex ring structure into a weakening smaller-scale vortex between 2110 and 2112 UTC cannot be determined with the 90-s temporal resolution that begins near 2111 UTC. It is possible that this new small-scale vortex originated from the enhanced vorticity present on the western periphery of the vortex ring (existing before 2111:47 UTC), which moves eastward relative to the expanding (~ 2 km wide) circulation.

The overall evolution of the vorticity field in the dual-Doppler analysis is qualitatively consistent with the evolution of the single-Doppler velocity fields observed by the radars. It is important to note that these analyses, with a radar horizon of ~ 100 m, are almost certainly missing a significant portion of the convergent surface layer at the tornado scale. Additionally, it should be noted that despite the close range of the radars to the tornado, we are unable to fully resolve the smallest scales of motion within it because of beam spreading. The four distinct vorticity maxima retrieved with the dual-Doppler analysis (Figs. 6g–j) are not easily discerned in the single-Doppler data; however, their development and motion can be tracked over the few minutes in which they are observed in the dual-Doppler data and they do not appear to be significantly sensitive to small changes in radar-pointing angle or smoothing (see the appendix).

Trajectory analysis

Instantaneous analyses, while illustrative, cannot be used to definitively determine source regions of air surrounding the tornado and mesocyclone. Trajectory analysis is necessary for this purpose. From approximately 2111 to 2117 UTC, trajectories are calculated

using the 3D wind data produced with smoothing set 1. Parcels are traced from origins in the inflow air east of the gust fronts and in the outflow air surrounding the mesocyclone, permitting the evaluation of the low-level storm-scale airflow in these important regions. Trajectories are computed using a fourth-order Runge–Kutta scheme with 20-s time steps. Temporal interpolation includes a term that translates the velocity field between dual-Doppler analyses, minimizing errors due to storm motion, particularly in areas containing large-velocity gradients. The vertical bounds of the dual-Doppler data, due to the close range of the radars to the storm, limit the trajectory analysis to only the lowest few kilometers AGL. The parcel trajectories are somewhat short because of the 6-min period of 3D dual-Doppler data available for their calculation. Sensitivities of the parcel trajectories to the radar alignment, the amount of smoothing performed, and the assumed wind profile between the ground and the lowest grid point are presented in the appendix.

1) STORM INFLOW TRAJECTORIES

A grid of parcels at $z = 150$ m AGL is tracked from the area just a few kilometers ahead of the gust fronts to evaluate storm inflow and the evolution of vertical vorticity for inflow parcels at 2110:44 UTC. These parcels experience strong ascent as they rise over the gust front on their way toward the vorticity maximum (Fig. 7). By 2115 UTC, all of the parcels reach the local vertical extent of dual-Doppler observations ($z \sim 1.0$ km), approximately 4 km ahead of the tornado. Observed values of vertical vorticity at parcel locations (Fig. 8a) significantly increase from their initial values ($< 0.005 \text{ s}^{-1}$) as they approach and rise over the rear-flank gust front; most parcel vertical vorticity begins to increase between 2112 and 2113 UTC, when positive values of tilting are observed at the parcel locations (Fig. 8d). Stretching (Fig. 8c) amplifies vertical vorticity at parcel positions, even when tilting is negative at some parcel locations after 2112:30 UTC.

While desirable, a complete diagnosis of the horizontal components of the vorticity equation is not possible with the present data, as a lack of thermodynamic observations precludes estimation of the baroclinic term, which is likely important in the horizontal buoyancy gradients along the gust fronts (e.g., Rotunno and Klemp 1985; Wicker and Wilhelmson 1995). Instead, a qualitative examination of the horizontal vorticity field is performed. An area-averaged hodograph that typifies the observed inflow to the storm (Fig. 5) indicates that approximately 45° of veering is present between $z = 150$ and 1350 m AGL and approximately 20° of backing is present between 1350 and 1950 m AGL, with

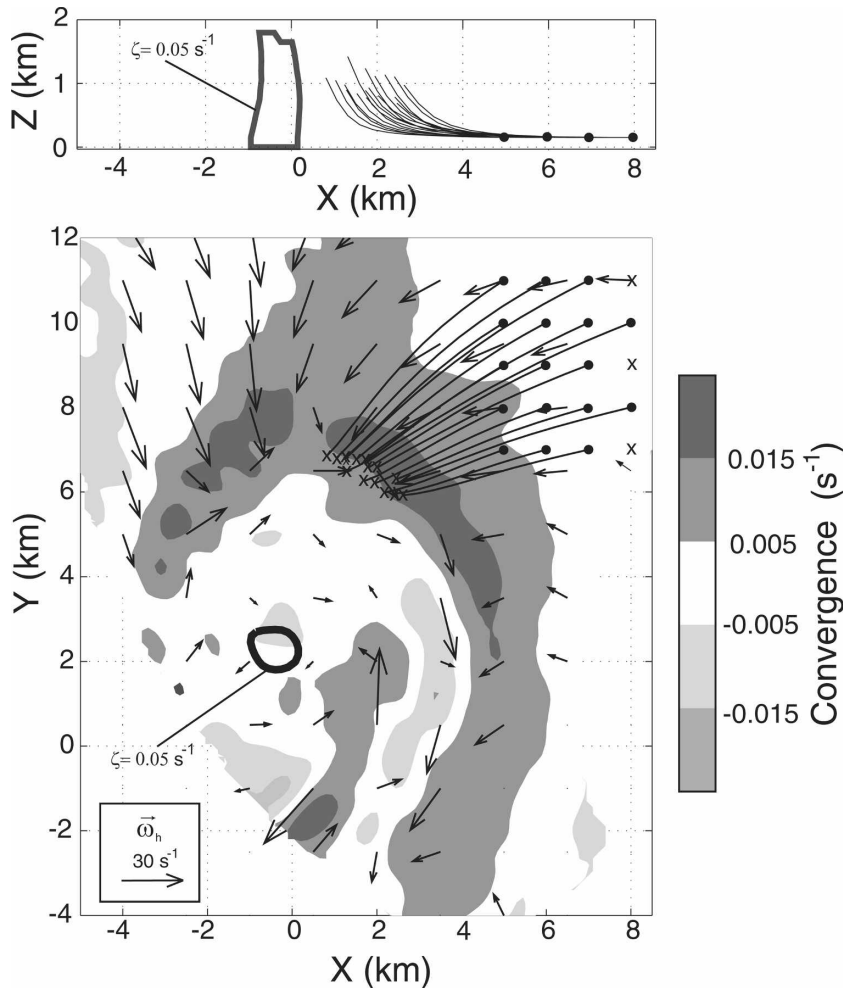


FIG. 7. Forward trajectory paths (in a storm-relative frame) that a grid of parcels (black dots) originating in the near-storm inflow at $z = 150$ m AGL at 2110:44 UTC transect over a 6-min integration period. (bottom) A horizontal cross section of convergence (shaded) at 300 m AGL, horizontal vorticity (vectors) at 600 m AGL, and vertical vorticity = 0.05 s^{-1} (black contour) at 2110:44 UTC; and (top) a projection of the 0.05 s^{-1} vertical vorticity contour and trajectory traces onto an x - z plane demonstrates the three dimensionality of the parcel paths. (bottom) An “X” marks the location in the x - y plane where a parcel exits the observed domain before the end of the integration period.

fairly constant wind speeds. As a result, the horizontal vorticity vector in the storm inflow is directed toward the tornado below 1350 m AGL, but away from it above 1350 m AGL. Parcel trajectories in the horizontal plane suggest a nearly streamwise storm-relative low-level flow, where “storm” motion refers to the average observed motion of the gust fronts and the vertical vorticity maximum. This orientation is optimal for the development of a rotating updraft through tilting.

2) TORNADIC AREA TRAJECTORIES

Two rings of parcels centered on the vertical vorticity maximum at ranges of 0.5 and 2.5 km are traced back-

ward in time from 2116:54 UTC at $z = 150$ m AGL in order to view the origins of air surrounding the tornado. Most parcels at the 2.5-km range diverge from the center of rotation and descend as they rotate around the vorticity maximum (Fig. 9). This motion is consistent with the presence of negatively buoyant outflow air or a dynamically driven downward-oriented perturbation pressure gradient force often found in the vicinity of the mesocyclone. A few parcels contract inward toward the vorticity maximum and ascend when they encounter convergence along the gust fronts. Parcels starting at the 0.5-km range to the resolved vertical vorticity maximum are observed to descend from as

Inflow environment

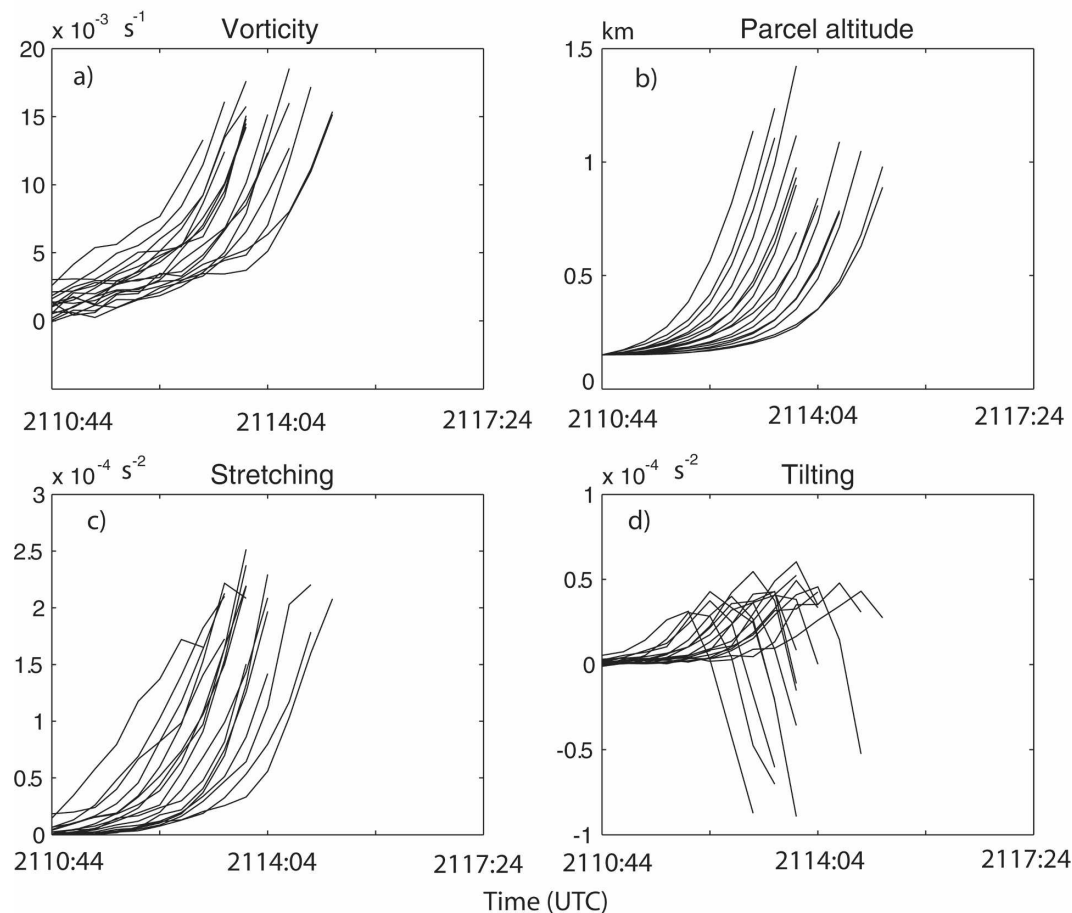


FIG. 8. (a) Vertical vorticity, (b) altitude, (c) vertical vorticity stretching, and (d) tilting of horizontal vorticity into the vertical observed at trajectory path locations in time for parcels originating in the storm inflow ahead of the gust fronts (shown in Fig. 7).

high as $z = 750$ m AGL and remain at an almost constant range to the vertical axis of rotation (Fig. 10). The plane of the material circuit on which these parcels lie does not uniformly descend, indicating that the plane is tilting with respect to the vertical. A similar trend of nonuniform descent is seen with parcels surrounding the vorticity maximum at $z = 150$ and 600 m AGL at 2113:53 UTC and $z = 600$ m AGL at 2116:54 UTC (not shown). The heights from which these parcels descend varies with changes in smoothing, radar alignment, or assumed wind at the surface, but the overall trend of descent is not changed (see the appendix).

The vorticity budget terms are not computed along parcel trajectories in this region because of the volatility of integrated stretching and tilting terms to even small errors in parcel residence times in these regions of large velocity gradients. However, individual stretching and tilting fields are shown in Fig. 11 for the dual-

Doppler analyses available between 2110:44 and 2115:37 UTC. Values of tilting are weaker than stretching at low levels, but become as significant at $z \geq 1$ km AGL. Negative stretching (compression) is found in some places along the rear-flank gust front where negative vertical vorticity is found, especially aloft.

3) REAR-FLANK TRAJECTORIES

A grid of parcels originating south and southwest of the tornado at 2110:44 UTC and $z = 750$ m AGL is traced forward in time in order to track the expected descent of outflow air on the rear-flank of the storm. While some parcels in this grid experience descent, others experience net ascent, exiting out of the top of the observation domain near the horizontal position of the vertical vorticity maximum (Fig. 12). The lack of thermodynamic data makes it difficult to diagnose why some parcels descend while others rise. Many of the

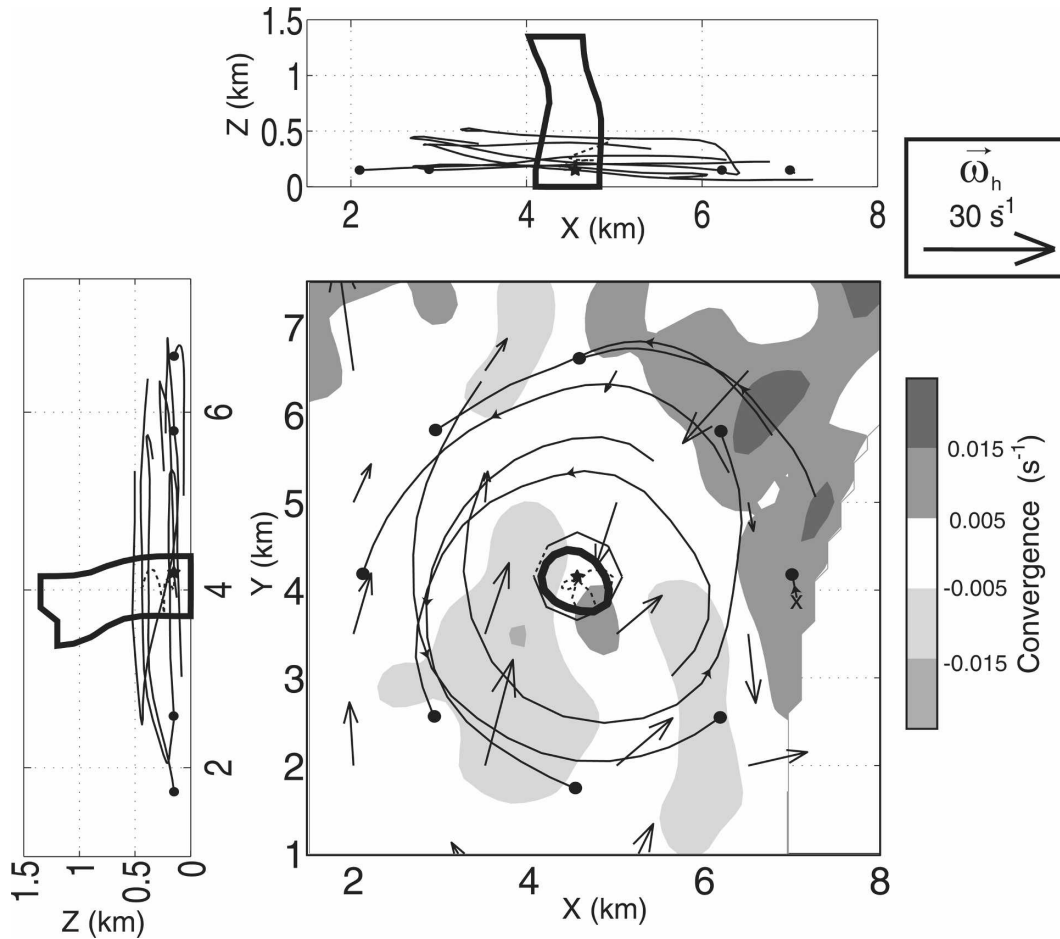


FIG. 9. As in Fig. 7, but for a 5-km-wide ring of parcels centered on the vertical vorticity maximum at 150 m AGL and traced backward in time from 2116:54 to 2110:44 UTC (arrow heads along trajectories in the x - y plane indicate the motion of the parcels forward in time; dots indicate parcel position at 2116:54 UTC). Convergence (shaded) and a vertical vorticity value of 0.05 s^{-1} (thick black contour) are shown at 2116:54 UTC. (left) A y - z projection of vertical vorticity and parcel trajectories are shown for additional 3D perspective. The black octagon centered on the vertical vorticity maximum in the x - y plane view shows the circuit of parcels tracked in Fig. 10. An “X” in the x - y plane marks the location where a parcel enters the observed domain during integration period.

rising parcels originating in the rear-flank region come from directly to the south and southeast of the vorticity maximum. It is possible that upward vertical motion along the secondary gust front, which is strong south-east of the tornado at the first few analysis times that are included in the trajectory integration, results in the ascent of some parcels, while others are descending in outflow downdrafts. Parcels originating within about 1.3 km of the vorticity maximum are observed to orbit it most rapidly, while parcels originating at a range >1.3 km south of the core of rotation either orbit it slowly or travel away from it toward the southeast. An average hodograph from the rear-flank region (Fig. 5) indicates northwesterly tornado-relative winds consistent with the departing motions of the parcels well south of the vorticity maximum.

5. Discussion

To summarize sections 3 and 4, two concentric circulations (~ 0.5 and ~ 2 km wide) existing at the beginning of data collection transition into one intermediate scale near the surface (although concentric scales are still observed aloft) that widens over the next several minutes. Subsequently, a multiple-vortex structure is observed with an asymmetric distribution of vertical vorticity such that discrete vorticity maxima are present on the western half of the circulation. After the disruption of the multiple-vortex structure, a new small-scale (~ 0.5 km wide) tornado forms. A schematic illustration of the observed evolution of the gust fronts and the vertical vorticity at low levels is illustrated in Fig. 13. Meteorological features observed during this evolution

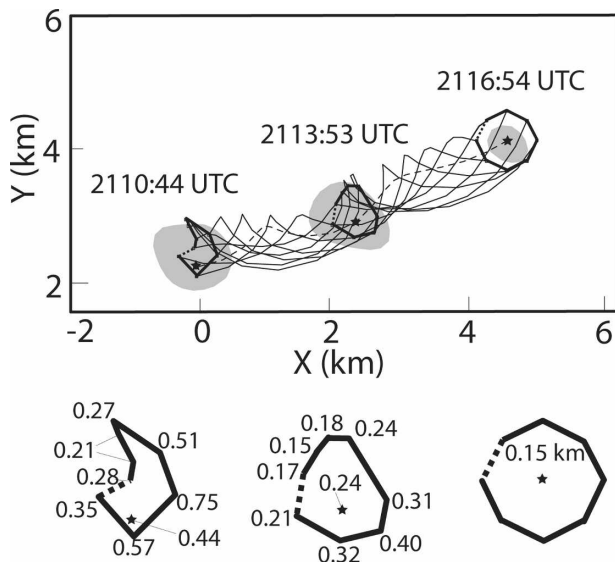


FIG. 10. Positions of a ring of parcels at 0.5-km range from the dual-Doppler vertical vorticity maximum originating at 2116:54 UTC at $z = 150$ m AGL traced backward in time to 2110:44 UTC. Trajectories are shown in a ground-relative frame. The horizontal plane projection of a material circuit connecting these parcels is shown with thick black lines and vertical vorticity >0.05 s^{-1} (shaded) are shown at three analysis times: 2116:54, 2113:53, and 2110:44 UTC. The horizontal plane projection of the material circuit at these 3 times is enlarged beneath with the heights AGL of each parcel labeled in kilometers. One line segment of the circuit is dashed to illustrate its orientation in the horizontal plane. The stars and the dashed trajectory trace the parcel at the center of the ring at 2116:54 UTC.

will now be related to past observed and simulated supercells and tornadoes.

a. Secondary gust front

A possible multiple gust front structure has been observed in at least a few other tornadic storms: one intercepted by the DOWs (Kiefer, Oklahoma; Wurman et al. 2007a), three observed with mobile mesonet data (e.g., Lee et al. 2004; Finley and Lee 2004; Markowski et al. 2002), and one in simulations by Adlerman (2003). The sharp horizontal wind shift observed in the present case is reminiscent of outflow surges documented by Lee et al. (2004) and Finley and Lee (2004), who found them to be associated with buoyancy gradients. However, no clear buoyancy gradient is evident across a possible secondary gust front evident as a wind shift and DOW reflectivity fine-line in the Dimmit storm (Fig. 7 from Markowski et al. 2002). No thermodynamic data were collected in the Crowell storm, which precludes a comparison of buoyancy fields to those seen in past studies, and also precludes evaluating their possible relevance to tornado maintenance (Markowski et al. 2002).

In the Kiefer storm, the northern end of the secondary gust front made contact with the primary rear-flank gust front (i.e., the outermost or easternmost rear-flank gust front) and was not observed to make contact with the convergence field immediately surrounding the tornado. In contrast, the convergence swath associated with the secondary rear-flank gust front in the present case is observed to make contact with the convergence field surrounding the tornado. When the Crowell secondary gust front discretely jumps to the east between 2112 and 2115 UTC, it quickly approaches the primary rear-flank gust front and partially merges with it shortly after it exits the dual-Doppler domain. It is possible that the difference between the observed tornado-relative positions of the secondary rear-flank gust fronts in the Crowell and Kiefer storms simply indicates they were sampled at different times in their evolution as they wrap cyclonically around the low-level vertical vorticity maximum.

b. Concentric scales of rotation

Concentric velocity couplets are observed to some degree between 2100 and 2117 UTC (e.g., $D = 400$ m and 2 km at 2100 UTC), each smaller than the meso-scale rotation ($D \geq 4$ km). The concentric scales of rotation are consistent with the “tornado” and “tornado–cyclone” circulations observed in some other DOW storm intercepts (e.g., Wurman et al. 1996; Wurman and Alexander 2004; Rasmussen and Straka 2007). Three-dimensional dual-Doppler data are not available when a steady configuration of concentric tornado/tornado–cyclone circulations is present (e.g., between 2100 and 2102 UTC), precluding the examination of the dynamics relevant to the coexistence of these scales. As mentioned in section 3, there is evidence of near-ground ($z = 150$ m AGL) convergence at the center of the concentric velocity couplets in the single-Doppler data at approximately 2102 UTC (Fig. 2b), which might indicate the contraction of low-level angular momentum associated with the tornado–cyclone. This contraction would result in an intensification of peak observed velocity closer to the axis of rotation which may be consistent with the intensification of the inner scale of rotation (tornado) near the surface due to the collapse of the corner flow region of a larger-scale of rotation (tornado–cyclone) as simulated in Lewellen and Lewellen (2007a,b).

c. Multiple-vortex structure

A core of divergence surrounded by a ring of convergence and vertical vorticity that is observed between 2108 and 2111 UTC is qualitatively consistent with the

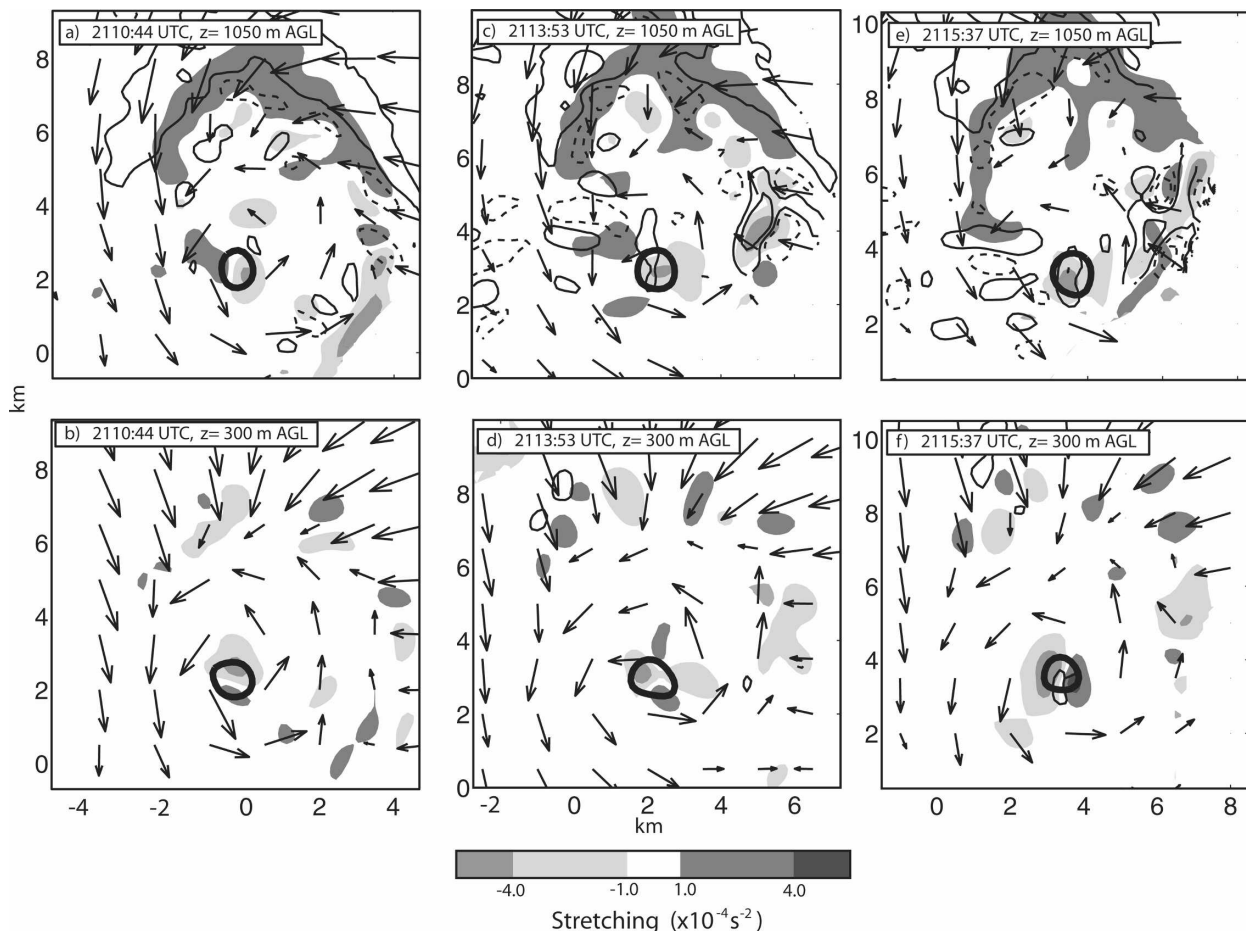


FIG. 11. Stretching (shaded), tilting (thin contours), and storm-relative wind (vectors) at $z =$ (top) 1.05 km AGL and (bottom) 300 m AGL at (a), (b) 2110:44, (c), (d) 2113:53, and (e), (f) 2115:35 UTC computed with smoothing set 1. The 0.05 s^{-1} vertical vorticity contour is shown with a thick black contour. Positive tilting of 1.0 and $4.0 \times 10^{-4} \text{ s}^{-2}$ is shown in thin solid contours and negative tilting of -1.0 and $-4.0 \times 10^{-4} \text{ s}^{-2}$ is shown in thin dashed contours.

familiar two-celled multiple-vortex tornado conceptual model (e.g., Davies-Jones et al. 2001) and is consistent with the end of the corner-flow collapse stages simulated in Lewellen and Lewellen (2007a). Three-dimensional dual-Doppler data are not available during the period for which this configuration is observed, precluding the verification of the vorticity structure in the vertical and the vertical perturbation pressure gradients retrieved (e.g., Hane and Ray 1985) in the core of rotation. The reason for the asymmetric distribution of vertical vorticity between 2107 and 2110 UTC is unknown; however, the evolution of the wind field surrounding the vortex suggests that the secondary gust front (an indication of locally surging outflow air and downdraft) played a role. The strong low-level convergence on the northwestern and northern periphery of the multiple-vortex circulation appears to be connected to the secondary gust front at 2109–2110 UTC (Figs.

6c,e,g,i), a period when the convergence directly on the eastern periphery of the vortex ring is weak and unorganized. It is possible that outflow air behind the secondary rear-flank gust front that is progressively wrapping around the low-level vorticity maximum (similar to the presumed evolution of the primary rear-flank gust front earlier in the lifetime of the storm) is disrupting the symmetry of the multiple-vortex structure. The presumed generation of the weak ~ 500 -m-wide vortex at 2111 UTC from vertical vorticity maxima orbiting the larger-scale circulation during the few minutes prior qualitatively resembles the production of a tornado in the Garden City, Kansas, supercell (Wakimoto and Liu 1998) from one of three small-scale vortices orbiting the mesocyclone.

The vorticity maxima on the western side of the vortex ring do not appear to significantly orbit the center of the ring during their development (2107:35–2109:08

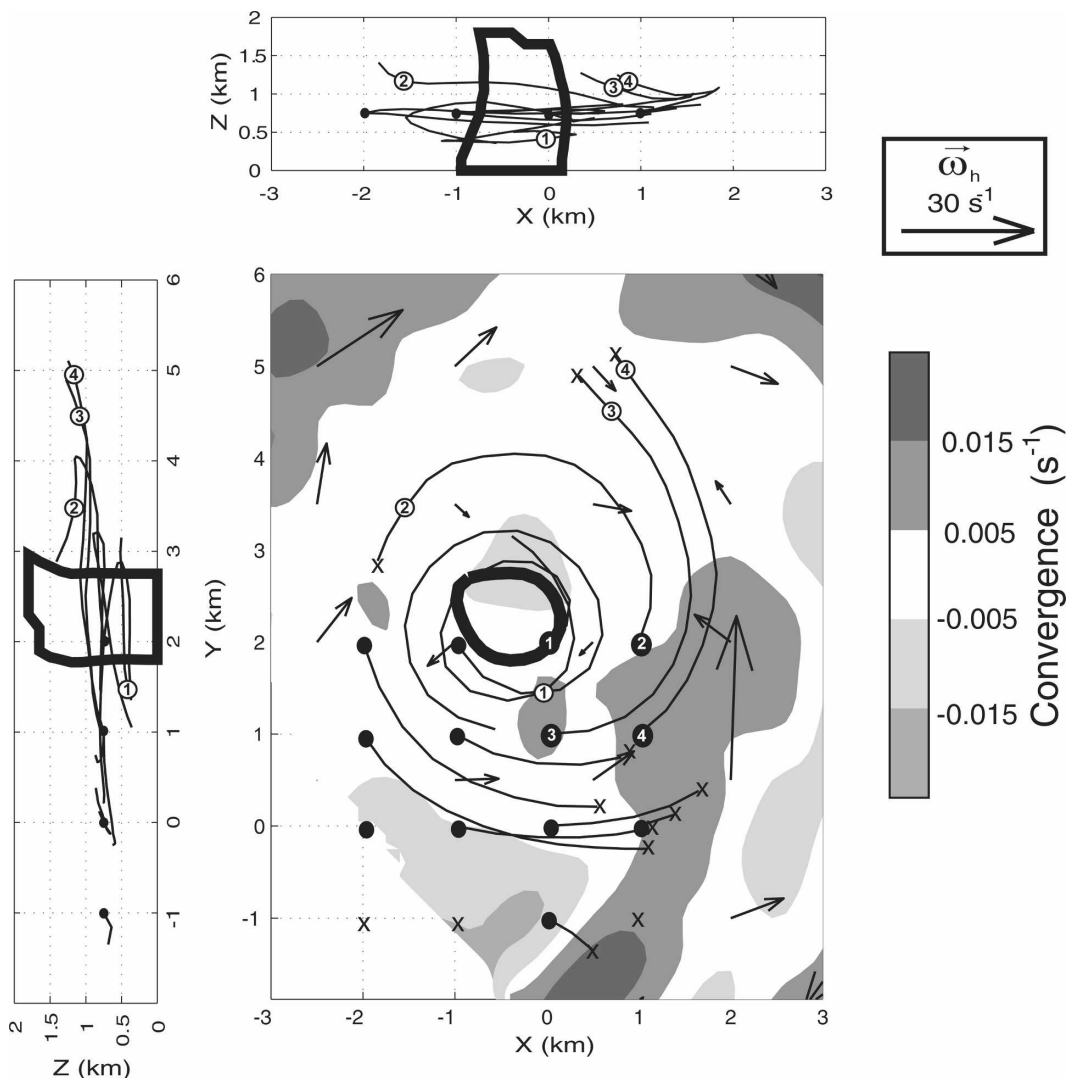


FIG. 12. As in Fig. 7, but for a grid of parcels originating at 2110:44 UTC at 750 m AGL in the observed portion of the rear flank just south of the tornado. The positions of four parcels referred to in section 5d are indicated with numbered dots at 2110:44 (black dots) and 2114:44 UTC (white dots).

UTC; Figs. 6c,e,g); however, after development (2109:08–2110:19 UTC; Figs. 6g,i), the vorticity maxima rotate cyclonically around the center of the vortex ring at different speeds. The two northernmost maxima at 2109:08 and 2110:19 UTC (A and B in Fig. 14) orbit around the vortex ring at a speed of $\sim 3.5 \text{ m s}^{-1}$ while the southern two (C and D) orbit at $\sim 7.5 \text{ m s}^{-1}$. The magnitude of the horizontal wind vector in the reference frame of the vortex ring varies as a function of azimuth because of the asymmetry of the flow; the ring-relative wind speed is generally greatest in the southern and western Hemispheres of the tornadic area of the storm due to the enhanced outflow winds there (at the times presented in Fig. 14). This may partly explain the different orbiting speeds of the four secondary vortices.

Ward (1972) and Wurman (2002) found secondary vortices in a multiple-vortex structure to be located in close proximity to the radius of maximum tangential velocity, whereas, Lewellen et al. (1997) found them inside of the radius of maximum swirl velocity. The secondary vorticity maxima as resolved in the present study with dual-Doppler data (smoothed) are located near, but a few hundred meters inside, the radius of maximum tangential wind on the southwest side of the vortex ring and likely contribute to the absolute maximum in observed tangential velocity. It is expected that the secondary vortices would travel with a component of the tangential wind speed in which they are embedded plus a component of upstream propagation (Rotunno 1984). A comparison of the motion of the secondary vortices

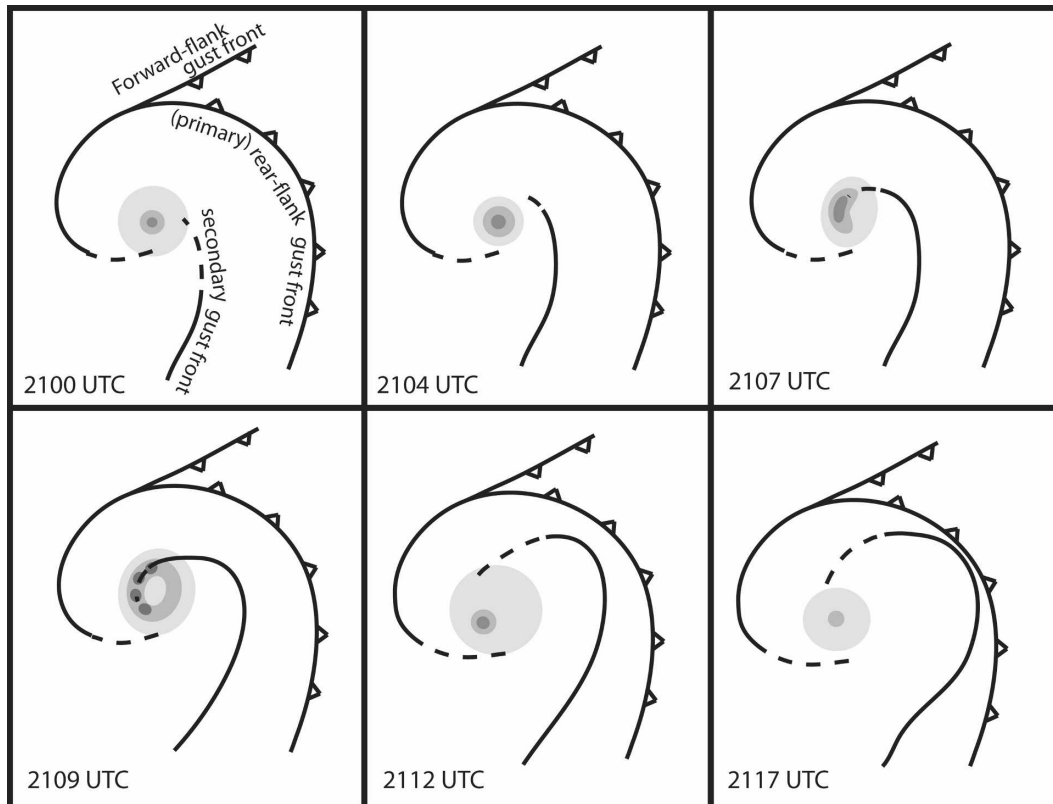


FIG. 13. A schematic illustration of the evolution of the primary and secondary gust fronts (black lines) and the vertical vorticity field (shaded) associated with the tornado and tornado-cyclone at low levels. Dashed lines indicate uncertainty in the position of the gust fronts. The approximate observation times are included.

relative to the observed swirl velocity of the overall multiple-vortex circulation is difficult because of the asymmetry of the flow and the difficulty in discerning a characteristic tangential advection velocity using single-Doppler (unsmoothed) data. The vorticity maxima are orbiting cyclonically around the vortex ring at approximately 20%–50% of the dual-Doppler (smoothed) tangential velocities observed in their core and 15%–30% of the maximum nearby tangential velocity. These orbiting motions are a bit slower than observed in previous studies (e.g., Wurman 2002; Lewellen et al. 1997; Ward 1972). This might suggest that upstream propagation significantly affected the motion of the secondary vortices.

d. Storm-scale flow

An increase in vertical vorticity due to tilting and stretching as parcels in the storm inflow rise along the gust fronts has been shown to be important to the supply of rotation in the low-level mesocyclone (e.g., Wicker and Wilhelmson 1995). The presence of a well-developed low-level mesoscale rotation (Fig. 21) is perhaps consistent with Wicker (1996) given that the low-

level horizontal vorticity vector just ahead of the storm is pointing in a similar direction as that in the forward-flank gust front region. However, in the present case, none of the parcels originating ahead of the storm are observed to spend time in the forward-flank gust front region where baroclinic generation of horizontal vorticity may be significant. This may be due to the small areal coverage of data in the environment ahead of the storm. We cannot assess whether parcels originating from the near-storm environment that rise over the rear-flank gust front during our observation period eventually reach the vicinity of the tornado. However, these parcel trajectories strongly suggest that air east of the gust front does not feed directly into the tornado at this stage. Dual-Doppler data available in the forward-flank of the storm also suggest a nearly streamwise flow below $z = 1$ km AGL (Fig. 5). Parcel trajectories originating at $z = 150$ m in the observed portion of the forward-flank region rise out of the domain in the upward motion along the forward-flank gust front and the occluded portion of the rear-flank gust front 3–4 km north of the tornado (not shown). However, insufficient wind data are available on the forward flank of the

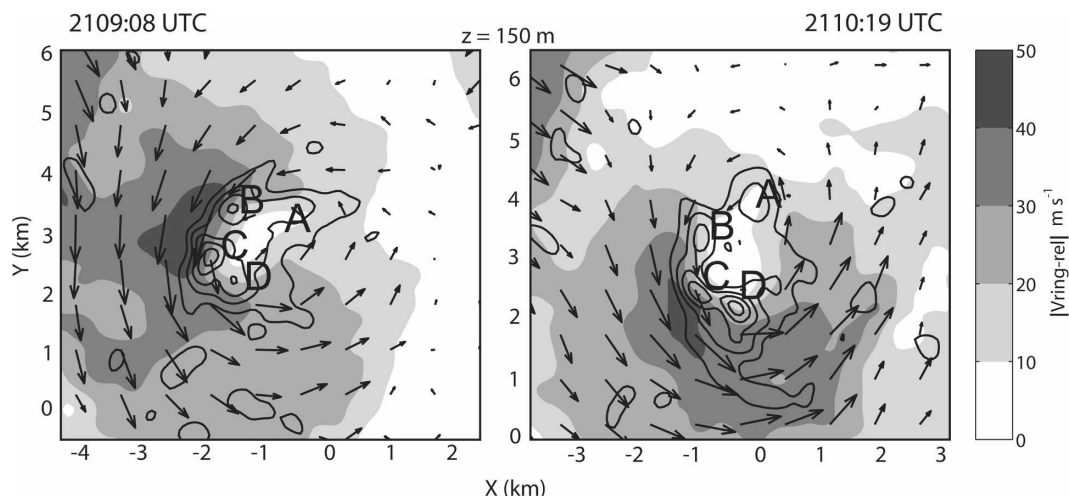


FIG. 14. Vertical vorticity (contours), winds relative to the motion of the center of the vorticity ring (vectors), and magnitude of the ring-relative wind (shaded) at $z = 150$ m AGL at (left) 2109:08 and (right) 2110:19 UTC using smoothing set 2. The outermost vorticity contour is 0.02 s^{-1} , incremented by 0.025 s^{-1} . Vorticity maxima are tracked with “A”–“D.”

storm to fully assess the importance of this region to the supply of vertical vorticity surrounding the tornado (e.g., Rotunno and Klemp 1985; Wicker and Wilhelmson 1995).

The presence of some outflow parcels that originate on the rear-flank and rise along the secondary gust front differs slightly from the typical conceptual model of descending rear-flank air that wraps around the tornado (e.g., Brandes 1978). The differential ascent of the rear-flank parcels (e.g., numbered parcels in Fig. 12) is perhaps illustrative of the airflow associated with the vortex line arch structure described in Straka et al. (2007) and Markowski et al. (2008). However, in those studies, vortex lines form the arch when they encounter convergence along the primary gust front and updraft, rather than being shaped by convergence within the outflow air as may occur in the present study. Analyses of 3D vortex lines for this and other DOW-observed storms will be performed in a future study as a tool to assess tornado maintenance.

The parcels in very close proximity to the vorticity maximum neither significantly converge toward, nor diverge away from, the center of rotation (Fig. 10). To assess the effects of scatterer centrifuging on this analysis, the deviant horizontal motion of hydrometeors or debris from the surrounding airflow is calculated using the simple parameterization of Das (1983):

$$u_p = \frac{v^2 v_t}{r g}, \quad (1)$$

where v is the tangential velocity at radius r from the center of rotation (modeled as a Rankine vortex), g is

gravity, and v_t is the terminal fall speed of the particle (Fig. 15a). Two sets of calculations are performed, one with values of v_{max} and r_{max} of the Rankine vortex equal to 23 m s^{-1} and 300 m , respectively, to assess centrifuging effects associated with the tornado, and one with v_{max} and r_{max} equal to 25 m s^{-1} and 1150 m , respectively, to assess centrifuging associated with the tornado–cyclone, both of which are observed for most of the trajectory analysis period (Fig. 4a). For the largest assumed particle size ($v_t = 10 \text{ m s}^{-1}$, consistent with large raindrops or small hailstones; Dowell et al. 2005), at $r = 500 \text{ m}$ the estimated divergence error due to particle centrifuging ($2u_p/r$; shown in Fig. 15b) associated with the tornado is 10% of the magnitude of divergence observed in the dual-Doppler syntheses, and at $r = 2.5 \text{ km}$, it is an even smaller fraction of the observed divergence in the outflow air and gust fronts surrounding the tornado–cyclone. These calculations indicate that the parcel trajectories shown in Figs. 9, 10, and 12 are likely not significantly affected by scatterer centrifuging, and the lack of significant horizontal contraction (spread) of parcels toward (away from) the vorticity maximum (Fig. 10) probably results from cyclostrophic balance above the surface layer. Data within the surface layer, if attainable, would likely show a very different convergence pattern.

The vertical distribution of the relative significance of the tilting and stretching terms near the tornado is similar to Dowell and Bluestein (2002). The shapes of these fields (except when a multiple-vortex structure is present) are generally consistent with observations from Wurman et al. (2007a,b), in that neighboring areas

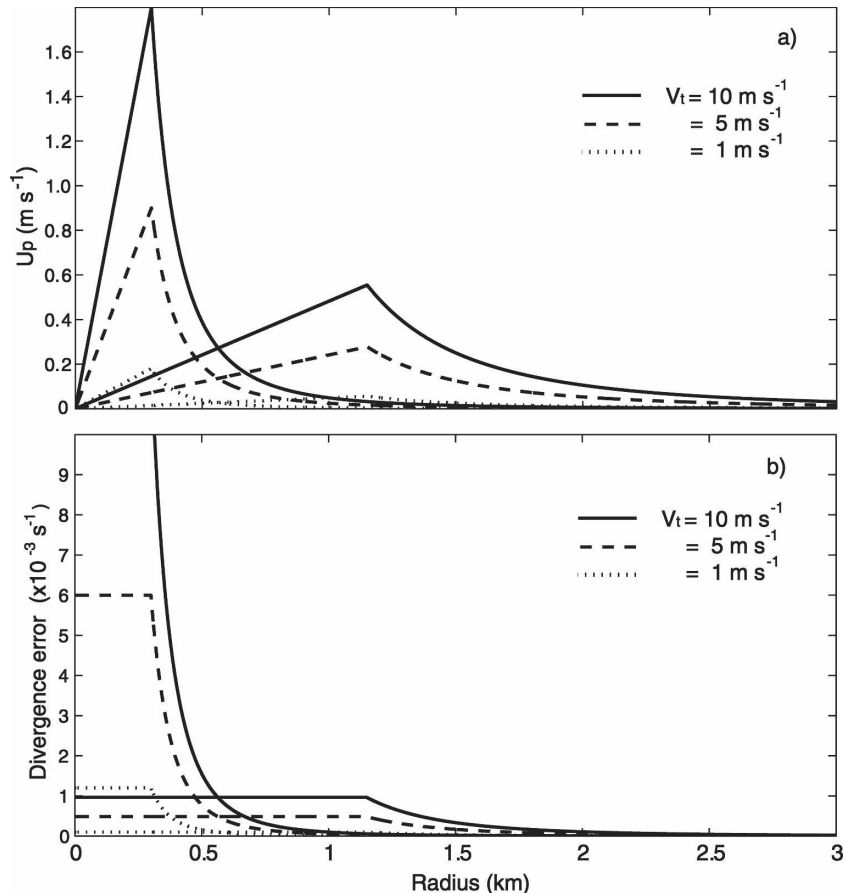


FIG. 15. (a) Radial particle motion and (b) the divergence error due to particle centrifuging associated with two Rankine vortices: one with $v_{\max} = 23 \text{ m s}^{-1}$ and $r_{\max} = 300 \text{ m}$, and one with $v_{\max} = 25 \text{ m s}^{-1}$ and $r_{\max} = 1150 \text{ m}$. Radial profiles are calculated for particles with three different terminal fall speeds: $v_t = 10$ (solid), 5 (dashed), and 1 m s^{-1} (dotted).

of intense divergence and convergence (and thus compression and stretching) are found in close proximity to the vorticity maximum. Of course, caution must be exercised when interpreting these results because the wind retrieval near the tornado can be somewhat sensitive to objective analysis choices, radar alignment errors, the typical dual-Doppler assumptions, and a lack of radar data in the lowest 150 m AGL (see the appendix). Similar retrieval errors may exist in these dual-Doppler cases because similar methods are employed in each.

6. Conclusions

Two Doppler-on-Wheels radars intercepted a tornadic supercell near the town of Crowell, Texas, on 30 April 2000. Data collected in this storm include single- and dual-Doppler analyses of sufficiently fine temporal and spatial resolution to reveal the low-level evolution

of both the partially resolved tornado and the well-resolved surrounding flow for several minutes. Interesting observations include the evolution of concentric scales of rotation, a brief multiple-vortex structure, and a secondary rear-flank gust front in the outflow air. The overall storm-scale flow surrounding the tornado is assessed using trajectory analysis.

The presence of concentric submesocyclone scales of rotation for certain periods of time in this and some other DOW-observed storms (e.g., Wurman and Alexander 2004) argues for further study of the interaction between these scales as well as a consistent taxonomy of tornado/tornado-cyclone vortices based on dynamical criteria [e.g., momentum profiles in Rasmussen and Straka (2007)] rather than only spatial scales (Agee et al. 1976). To solidify our understanding of the dynamics governing the coexistence of these concentric vortices, more high-resolution radar data and numerical simula-

tions resolving spatial scales equal to a few hundred meters must be analyzed.

The short-lived nature of the multiple-vortex structure and the inconsistencies in secondary-vortex-orbiting motion when compared to past studies may have been influenced by the asymmetry of the storm-scale flow surrounding it. The flow asymmetry in this case was generated by a surge of outflow air in close proximity to the tornado. A continued focus on the effects of asymmetric background storm-scale flow on tornado behavior will likely advance our knowledge of vortex stability and damage potential.

A double rear-flank gust front structure is observed in this storm, consistent with multiple surges of thunderstorm outflow. To our knowledge, a documentation of possible secondary rear-flank gust fronts has only been published in data collected or simulated in five other supercell storms. It is unknown whether such a paucity of documentation is due to a lack of high-resolution storm observations, or if multiple gust fronts are not common to supercell storms. The secondary gust front observed in the present case appears to have affected the convergence field surrounding the tornado, and, thus, might have played an important but previously undocumented role in its evolution. Because of the possible influence they have on tornado behavior, future studies that examine the tornadic area of observed or simulated supercells should look for multiple gust front structures in an effort to determine the dynamics governing their generation and the percentage of storms in which they are present and play a significant role.

The examination of similar high-resolution single- and dual-Doppler data collected in additional tornadic supercells will prove useful in determining the consistency of the possible influences of storm-scale flow on tornado behavior. While much information can be derived from these data, the 90-s temporal resolution that is available at certain times is too coarse to unambiguously track features with spatial scales smaller than a few hundred meters. The use of 3D data with very fine (~ 10 s) temporal resolution, such as that achievable by the rapid-scan Doppler-on-Wheels radar (Wurman and Randall 2001), would provide valuable details of the kinematic fields surrounding the tornado.

Acknowledgments. This work was supported with NSF Grants ATM-0437512 and ATM-0437505. The authors thank Curtis Alexander, David Dowell, Mario Majcen, Jeffrey Frame, and Zack Byko for helpful analysis discussion; two anonymous reviewers for their suggestions on how to improve an earlier version of this manuscript; C. Alexander, Paul Robinson, and

Nettie Arnott for analysis scripts and support; and the ROTATE 2000 crew members for the data collection itself.

APPENDIX

Sensitivity Analysis of Wind Retrievals and Trajectory Calculations

The sensitivities of the kinematic fields and trajectory analyses presented in this study to certain parameters employed in the dual-Doppler wind synthesis are evaluated using two series of experiments. Individual parameters whose sensitivities are studied include radar alignment accuracy, the extrapolation assumptions of horizontal wind downward to the ground to implement the lower boundary condition, and the smoothing parameters of the single-Doppler fields. These parameter choices all involve some amount of subjectivity and have been observed by the authors to affect the synthesized structure of other DOW-observed vortices and the convergence fields surrounding them.

Three sensitivity experiments are performed to test the finescale vorticity and convergence structure of the tornadic circulation at the time presented in Fig. 6i, the time at which perhaps the most intricate finescale detail of the vortex is observed. In these experiments, the following conditions are imposed: 1) the smoothing and wind synthesis are performed with the method described in section 2 using smoothing set 2; 2) same as experiment 1, but that $\kappa = 0.023 \text{ km}^2$; and 3) same as experiment 1, but that the single-Doppler data collected by DOW3 are rotated 0.5° clockwise from our best-estimate ground clutter alignment result. The choice of κ in experiment 2 is somewhat arbitrary, but corresponds to a theoretical response function for Barnes smoothing ("accuracy index," D , in Barnes 1964) of $D = 0.8$ for $\lambda = 1 \text{ km}$ (roughly half of the width of the tornado cyclone circulation). The decrease in κ is chosen to address the possibility that meteorological features are being oversmoothed in our analyses. The radar alignment perturbation of 0.5° used in experiment 3 also is somewhat arbitrary, but represents roughly twice the presumed accuracy attained by the method described in section 2. The subtle differences in vorticity and convergence fields that are observed when comparing all three sensitivity experiments (Fig. A1) do not affect the qualitative interpretation of the tornado/tornado-cyclone structure discussed in sections 4 and 5.

Four additional experiments are conducted to test the sensitivity of the observed storm-scale flow to smoothing, radar alignment, and the assumed wind profile in the surface layer: 1) the smoothing and wind

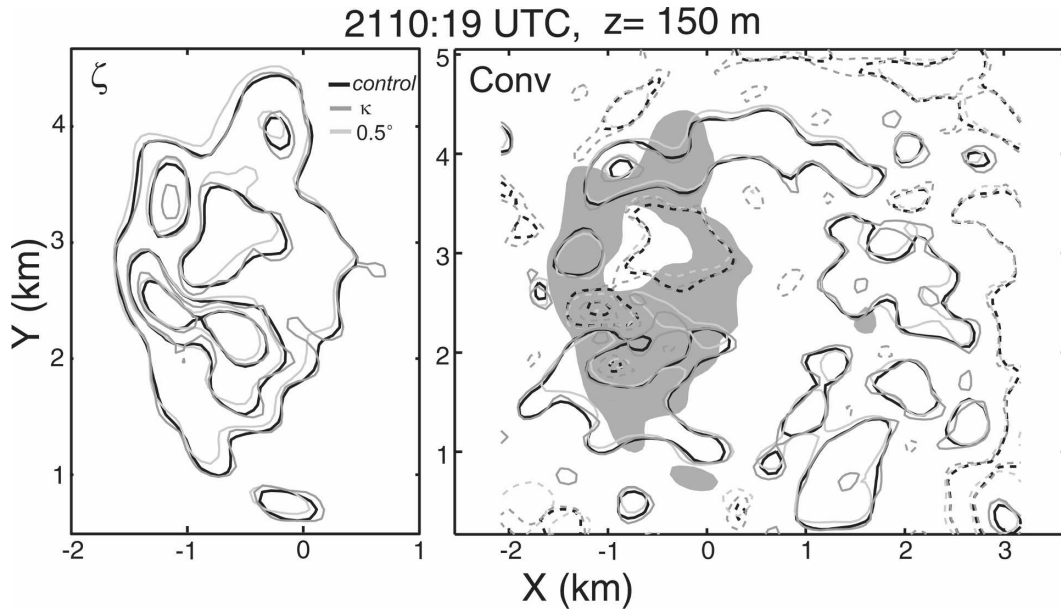


FIG. A1. (left) Vertical vorticity contours of 0.03, 0.06, and 0.09 s^{-1} at $z = 150$ m AGL at 2110:19 UTC for tornado-scale sensitivity experiment 1 (“control”), experiment 2 (“ κ ”), and experiment 3 (“ 0.5° ”). (right) Convergence contours of -0.035 , -0.01 , 0.01 , and 0.035 s^{-1} at the same height, time, and for the same experiments as in the left panel. Negative values of convergence are dashed. For reference, vertical vorticity $>0.03 \text{ s}^{-1}$ from the control experiment is shaded in the right panel.

synthesis are performed with the method described in section 2 using smoothing set 1; 2) same as experiment 1, but that $\kappa = 0.09 \text{ km}^2$ (chosen such that $D = 0.8$ for $\lambda = 2 \text{ km}$ rather than $D \approx 0.63$ for experiment 1); 3) same as experiment 1, but that the single-Doppler data collected by DOW3 are rotated 0.5° clockwise from the ground clutter alignment result; and 4) same as experiment 1, but that $u = v = 0$ at $z = 0$. The storm-scale vertical motion and vertical vorticity at $z = 1 \text{ km}$ AGL produced by each of the four experiments at 2110:44 UTC are shown in Fig. A2. The magnitude of the vertical vorticity maximum shows the greatest difference comparing experiment 2 to experiment 1 (an increase on average by 16%). In contrast, experiments 3 and 4 differ from experiment 1 by $<1\%$. The overall pattern of w along the gust fronts and in the outflow air among all four experiments is insensitive to the tested parameters, and the observed magnitudes of w vary by $<0.5 \text{ m s}^{-1}$ on average at any point among experiments 1–3. Unsurprisingly, the magnitudes of w are smallest in experiment 4 because zero convergence is prescribed below 150 m AGL; the magnitude varies by as much as 1 m s^{-1} on average from experiment 1. Furthermore, isolated w maxima or minima within 1–3 km of the vertical vorticity maximum are the most sensitive to the tested synthesis parameters, with variations in this region of 1–4 m s^{-1} among the four experiments. Experiment 2

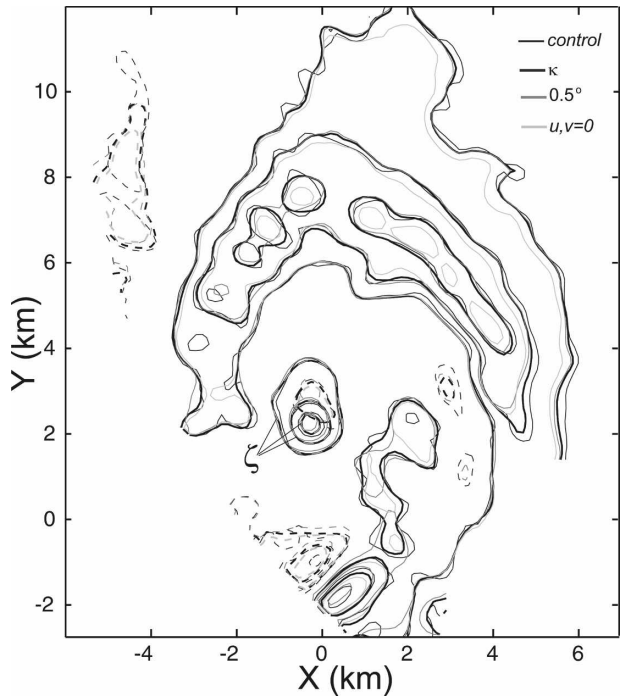


FIG. A2. Vertical velocity at $z = 1 \text{ km}$ AGL at 2110:44 UTC for storm-scale sensitivity experiment 1 (“control”), experiment 2 (“ κ ”), experiment 3 (“ 0.5° ”), and experiment 4 (“ $u, v = 0$ ”). Dashed contours are $w = -10$ and -5 m s^{-1} ; solid contours are $w = 15$, 10 , and 5 m s^{-1} . Three closed contours of $\zeta = 0.03$, 0.05 , and 0.07 s^{-1} located at $z = 1 \text{ km}$ AGL are shown for each of the four experiments (ζ maximum is located at $x = -0.3 \text{ km}$, $y = 2.3 \text{ km}$).

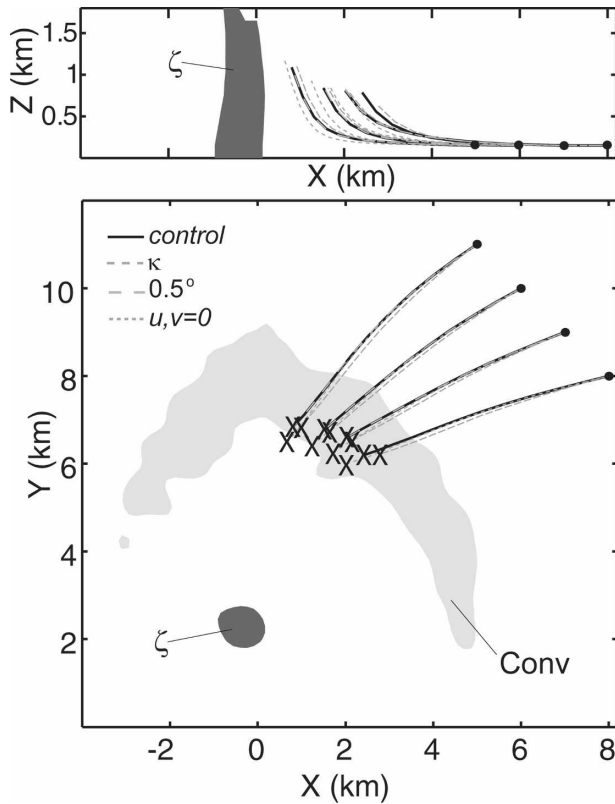


FIG. A3. Four storm-relative parcel trajectories projected onto (top) an x - z plane and (bottom) an x - y plane selected from a grid of parcels with origins identical to those shown in Fig. 7 and traced forward in time from 2110:44 to 2116:54 UTC using wind fields produced by storm-scale sensitivity experiment 1 (“control”), experiment 2 (“ κ ”), experiment 3 (“ 0.5° ”), and experiment 4 (“ $u, v = 0$ ”). For reference, convergence along the primary gust fronts $>0.012 \text{ s}^{-1}$ at $z = 300 \text{ m}$ AGL is shaded in light gray in the bottom panel and vertical vorticity $>0.05 \text{ s}^{-1}$ is shaded in dark gray in both panels ($z = 300 \text{ m}$ AGL for the bottom panel) from 2110:44 UTC. An “X” in the bottom panel marks the location in the x - y plane where a parcel exits the observed domain before the end of the integration period.

shows the greatest differences relative to experiment 1 in this area of the storm.

To see the impact of these velocity differences on our trajectory calculations, these were redone using the set of storm-scale sensitivity experiments. As expected, differences in magnitude of vertical motion along the gust fronts among the four experiments lead to differences in parcel position along trajectories traced from identical origins near the ground in the inflow environment at 2110:44 UTC (Fig. A3). The greatest disparity in parcel positions from experiment 1 (those shown in Fig. 7) occur in experiment 4, where the lessened w along the gust fronts results in parcels that reach the top of the domain at a later time than in the other three experiments. However, differences in these trajectories do not

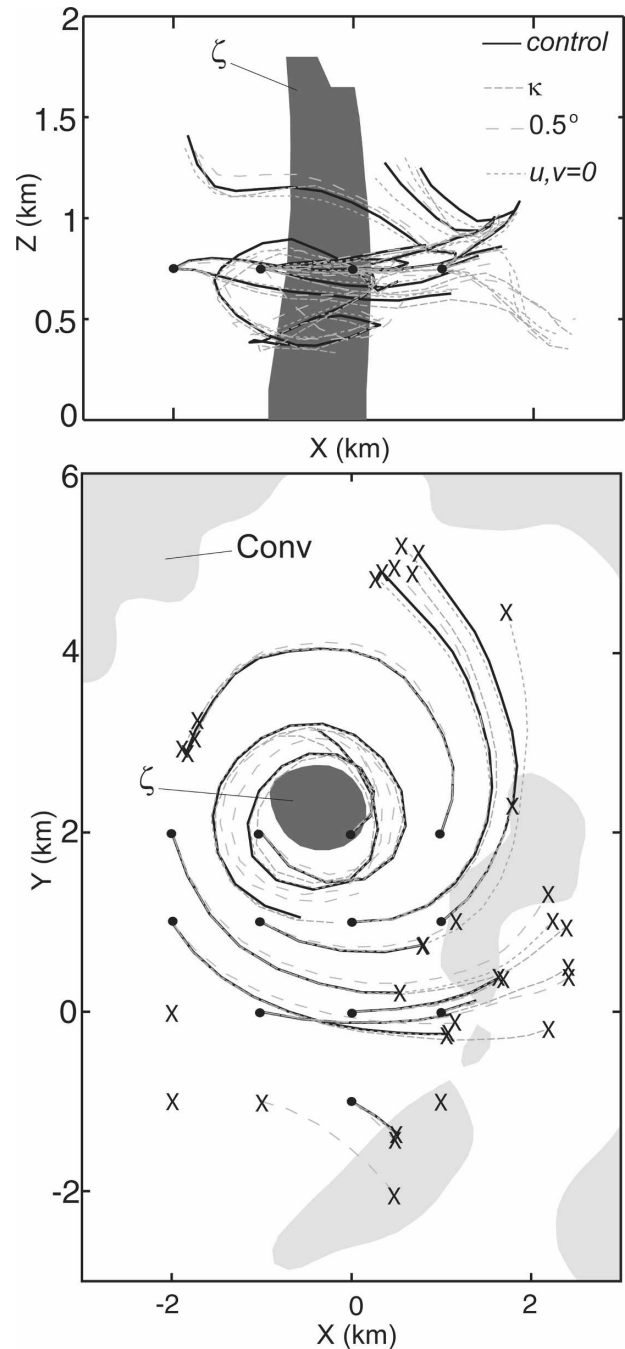


FIG. A4. Storm-relative parcel trajectories projected onto (top) an x - z plane and (bottom) an x - y plane from a grid of parcels with origins identical to those shown in Fig. 12 and traced forward in time from 2110:44 to 2116:54 UTC using wind fields produced by storm-scale sensitivity experiment 1 (“control”), experiment 2 (“ κ ”), experiment 3 (“ 0.5° ”), and experiment 4 (“ $u, v = 0$ ”). For reference, convergence along the gust fronts $>0.008 \text{ s}^{-1}$ at $z = 300 \text{ m}$ AGL is shaded in light gray in the bottom panel and vertical vorticity $>0.05 \text{ s}^{-1}$ is shaded in dark gray in both panels ($z = 300 \text{ m}$ AGL for the bottom panel) at 2110:44 UTC. An “X” in the bottom panel marks the location in the x - y plane where a parcel exits the observed domain before the end of the integration period.

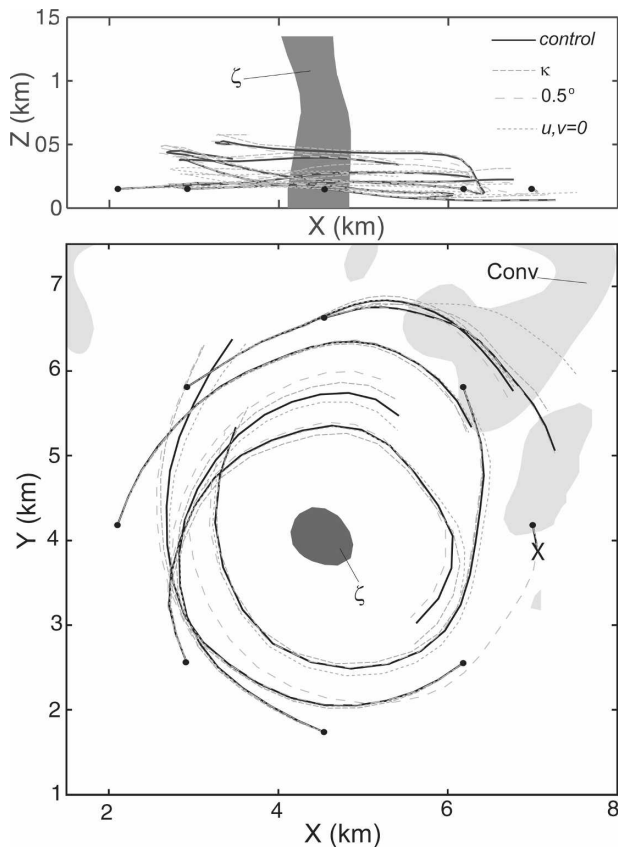


FIG. A5. Storm-relative parcel trajectories projected onto (top) an x - z plane and (bottom) an x - y plane from a 5-km-wide ring of parcels with origins identical to those shown in Fig. 9 and traced backward in time from 2116:54 to 2110:44 UTC using wind fields produced by storm-scale sensitivity experiment 1 (“control”), experiment 2 (“ κ ”), experiment 3 (“0.5°”), and experiment 4 (“ $u, v = 0$ ”). For reference, convergence along the primary gust fronts $>0.008 \text{ s}^{-1}$ at $z = 300 \text{ m}$ AGL is shaded in light gray in the bottom panel and vertical vorticity $>0.05 \text{ s}^{-1}$ is shaded in dark gray in both panels ($z = 300 \text{ m}$ AGL for the bottom panel) at 2116:54 UTC. An “X” in the x - y plane marks the location where a parcel enters the observed domain during the integration period.

affect the qualitative interpretation of the storm inflow. Most parcels with identical origins on the rear flank of the storm at 2110:44 UTC and $z = 750 \text{ m}$ AGL in experiments 2–4 (Fig. A4) exhibit minor differences in horizontal position in time with those from experiment 1 (those shown in Fig. 12). The largest of these differences ($\sim 700 \text{ m}$) occurs in the two parcels that originate closest to the vertical vorticity maximum, where the greatest overall differences among the experiments are observed in the kinematic fields. However, these differences do not affect the interpretation described in sections 4 and 5, as both parcels in all experiments orbit the vorticity maximum and have similar heights AGL in time. Vertical positions of parcels along all rear-flank

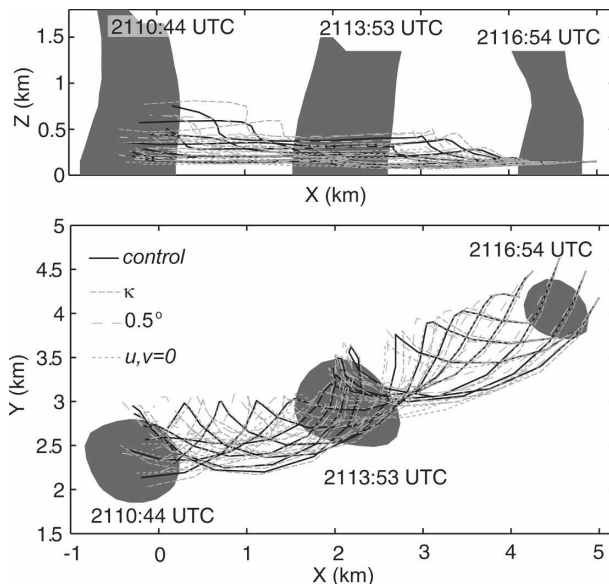


FIG. A6. Ground-relative parcel trajectories projected onto (top) an x - z plane and (bottom) an x - y plane from a 1-km-wide ring of parcels with origins identical to those shown in Fig. 10 and traced backward in time from 2116:54 to 2110:44 UTC using wind fields produced by storm-scale sensitivity experiment 1 (“control”), experiment 2 (“ κ ”), experiment 3 (“0.5°”), and experiment 4 (“ $u, v = 0$ ”). For reference, vertical vorticity $>0.05 \text{ s}^{-1}$ is shaded in both panels (at $z = 300 \text{ m}$ AGL for the bottom panel) at 2110:44, 2113:53, and 2116:54 UTC.

trajectories in the four experiments are similar in time with interexperiment differences between like parcels of less than 100 m; therefore, no qualitative differences in rear-flank airflow are observed because of the tested sensitivities. Parcels traced backward in time at a distance of 2.5 km from the vorticity maximum (those shown in Fig. 9) are qualitatively similar among all experiments (Fig. A5). Differences in horizontal positions of like parcels in time are as much as 1 km for a few parcels, but are typically less than 300 m. Parcels in experiment 4 experience the lowest rates of ascent or descent, but parcels in all experiments undergo ascent or descent at similar times, and differences in the vertical positions among the experiments are less than 200 m at the final integration time. Unsurprisingly, trajectories in the 1-km-wide ring surrounding the vertical vorticity maximum (those shown in Fig. 10) are the most sensitive to the three experiments performed (Fig. A6). Differences in the horizontal and vertical positions of some of these parcels, when compared with identical parcels in experiment 1, are as large as 600 and 300 m, respectively. However, in all experiments most parcels descend at qualitatively similar rates as they rotate around the vorticity maximum.

Overall, the differences in parcel trajectories among

the sensitivity experiments performed do not change the qualitative interpretation of the airflow presented in sections 4 and 5. Such sensitivities may be more critical to consider when integrating parcel trajectories over longer time periods than are possible in this study.

REFERENCES

- Adlerman, E. J., 2003: Numerical simulations of cyclic storm behavior: Mesocyclogenesis and tornadogenesis. Ph.D. dissertation, University of Oklahoma, 217 pp. [Available from School of Meteorology, University of Oklahoma, 100 East Boyd, Suite 1310, Norman, OK 73019.]
- Agee, E. M., J. T. Snow, and P. R. Clare, 1976: Multiple vortex features in the tornado cyclone and the occurrence of tornado families. *Mon. Wea. Rev.*, **104**, 552–563.
- Alexander, C. R., and J. Wurman, 2005: The 30 May 1998 Spencer, South Dakota, storm. Part I: The evolution and environment of the tornadoes. *Mon. Wea. Rev.*, **133**, 72–96.
- Barnes, S. L., 1964: A technique for maximizing details in numerical weather map analysis. *J. Appl. Meteor.*, **3**, 396–409.
- Bluestein, H. B., and A. L. Pazmany, 2000: Observations of tornadoes and other convective phenomena with a mobile, 3-mm wavelength, Doppler radar: The spring 1999 field experiment. *Bull. Amer. Meteor. Soc.*, **81**, 2939–2951.
- , C. C. Weiss, and A. L. Pazmany, 2003: Mobile Doppler radar observations of a tornado in a supercell near Bassett, Nebraska, on 5 June 1999. Part I: Tornadogenesis. *Mon. Wea. Rev.*, **131**, 2954–2967.
- , —, and —, 2004: The vertical structure of a tornado: High-resolution, W-band, Doppler radar observations near Happy, Texas, on 5 May 2002. *Mon. Wea. Rev.*, **132**, 2325–2337.
- Brandes, E. A., 1977: Gust front evolution and tornado genesis as viewed by Doppler radar. *J. Appl. Meteor.*, **16**, 333–338.
- , 1978: Mesocyclone evolution and tornadogenesis: Some observations. *Mon. Wea. Rev.*, **106**, 995–1011.
- , 1981: Fine structure of the Del City–Edmond tornadic mesocirculation. *Mon. Wea. Rev.*, **109**, 635–647.
- , 1984: Vertical vorticity generation and mesocyclone sustenance in tornadic thunderstorms: The observational evidence. *Mon. Wea. Rev.*, **112**, 2253–2269.
- Das, P., 1983: Vorticity concentration in the subcloud layers of a rotating cloud. National Science Foundation Final Rep. ATM-8023825, 78 pp.
- Davies-Jones, R., 1973: The dependence of core radius swirl ratio in a tornado simulator. *J. Atmos. Sci.*, **30**, 1427–1430.
- , R. J. Trapp, and H. B. Bluestein, 2001: Tornadoes and tornadic storms. *Severe Convective Storms, Meteor. Monogr.*, No. 50, Amer. Meteor. Soc., 167–221.
- Dessens, J., 1972: Influence of ground roughness on tornadoes: A laboratory simulation. *J. Appl. Meteor.*, **11**, 72–75.
- Dowell, D. C., and H. B. Bluestein, 1997: The Arcadia, Oklahoma, storm of 17 May 1981: Analysis of a supercell during tornadogenesis. *Mon. Wea. Rev.*, **125**, 2562–2582.
- , and —, 2002: The 8 June 1995 McLean, Texas, storm. Part II: Cyclic tornado formation, maintenance, and dissipation. *Mon. Wea. Rev.*, **130**, 2649–2670.
- , Y. Richardson, and J. Wurman, 2002: Observations of the formation of low-level rotation: The 5 June 2001 Sumner County, Kansas, tornado. Preprints, *21st Conf. on Severe Local Storms*, San Antonio, TX, Amer. Meteor. Soc., 12.3. [Available online at <http://ams.confex.com/ams/pdfpapers/47335.pdf>.]
- , C. R. Alexander, J. M. Wurman, and L. J. Wicker, 2005: Centrifuging of hydrometeors and debris in tornadoes: Radar-reflectivity patterns and wind-measurement errors. *Mon. Wea. Rev.*, **133**, 1501–1524.
- Finley, C. A., and B. D. Lee, 2004: High-resolution mobile mesonet observations of RFD surges in the June 9 Bassett, Nebraska supercell during Project ANSWERS 2003. Preprints, *22nd Conf. on Severe Local Storms*, Hyannis, MA, Amer. Meteor. Soc., CD-ROM, P11.3. [Available online at <http://ams.confex.com/ams/pdfpapers/82005.pdf>.]
- Grasso, L. D., and W. R. Cotton, 1995: Numerical simulation of a tornado vortex. *J. Atmos. Sci.*, **52**, 1192–1203.
- Hane, C. E., and P. S. Ray, 1985: Pressure and buoyancy fields derived from Doppler radar data in a tornadic thunderstorm. *J. Atmos. Sci.*, **42**, 18–35.
- Klemp, J. B., and R. Rotunno, 1983: A study of the tornadic region within a supercell thunderstorm. *J. Atmos. Sci.*, **40**, 359–377.
- Koch, S. E., M. DesJardins, and P. J. Kocin, 1983: An interactive Barnes objective map analysis scheme for use with satellite and conventional data. *J. Climate Appl. Meteor.*, **22**, 1487–1503.
- Lee, B. D., C. A. Finley, and P. Skinner, 2004: Thermodynamic and kinematic analysis of multiple RFD surges for the 24 June 2003 Manchester, South Dakota cyclic tornadic supercell during Project ANSWERS 2003. Preprints, *22nd Conf. on Severe Local Storms*, Hyannis, MA, Amer. Meteor. Soc., P11.2. [Available online at <http://ams.confex.com/ams/pdfpapers/82000.pdf>.]
- Lee, W.-C., and J. Wurman, 2005: The diagnosed structure of the Mulhall tornado. *J. Atmos. Sci.*, **62**, 2373–2393.
- Lemon, L. R., and C. A. Doswell, 1979: Severe thunderstorm evolution and mesocyclone structure as related to tornadogenesis. *Mon. Wea. Rev.*, **107**, 1184–1197.
- Lewellen, D. C., and W. S. Lewellen, 2007a: Near-surface intensification of tornado vortices. *J. Atmos. Sci.*, **64**, 2176–2194.
- , and —, 2007b: Near-surface vortex intensification through corner flow collapse. *J. Atmos. Sci.*, **64**, 2195–2209.
- , —, and J. Xia, 2000: The influence of a local swirl ratio on tornado intensification near the surface. *J. Atmos. Sci.*, **57**, 527–544.
- Lewellen, W. S., D. C. Lewellen, and R. I. Sykes, 1997: Large-eddy simulation of a tornado's interaction with the surface. *J. Atmos. Sci.*, **54**, 581–605.
- Markowski, P. M., 2002: Hook echoes and rear-flank downdrafts: A review. *Mon. Wea. Rev.*, **130**, 852–876.
- , J. M. Straka, and E. N. Rasmussen, 2002: Direct surface thermodynamic observations within the rear-flank downdrafts of nontornadic and tornadic supercells. *Mon. Wea. Rev.*, **130**, 1692–1721.
- , E. Rasmussen, J. Straka, R. Davies-Jones, Y. Richardson, and R. J. Trapp, 2008: Vortex lines within low-level mesocyclones obtained from pseudo-dual-Doppler radar observations. *Mon. Wea. Rev.*, **136**, 3513–3535.
- Pauley, P. M., and X. Wu, 1990: The theoretical, discrete, and actual response of the Barnes objective analysis scheme for one- and two-dimensional fields. *Mon. Wea. Rev.*, **118**, 1145–1163.

- Rasmussen, E. N., and J. M. Straka, 2007: Evolution of low-level angular momentum in the 2 June 1995 Dimmitt, Texas, tornado cyclone. *J. Atmos. Sci.*, **64**, 1365–1378.
- , —, R. Davies-Jones, C. A. Doswell III, F. H. Carr, M. D. Eilts, and D. R. MacGorman, 1994: Verification of the Origins of Rotation in Tornadoes Experiment: VORTEX. *Bull. Amer. Meteor. Soc.*, **75**, 995–1006.
- Richardson, Y., D. Dowell, and J. Wurman, 2001: High resolution dual-Doppler analyses of two thunderstorms during the pre-tornadogenesis and mature tornado stages. Preprints, *30th Int. Conf. on Radar Meteorology*, Munich, Germany, Amer. Meteor. Soc., 295–297.
- Rotunno, R., 1984: An investigation of a three-dimensional asymmetric vortex. *J. Atmos. Sci.*, **41**, 283–298.
- , and J. B. Klemp, 1985: On the rotation and propagation of simulated supercell thunderstorms. *J. Atmos. Sci.*, **42**, 271–292.
- Straka, J. M., E. N. Rasmussen, R. P. Davies-Jones, and P. M. Markowski, 2007: An observational and idealized numerical examination of low-level counter-rotating vortices in the rear flank of supercells. *Electron. J. Severe Storms Meteor.*, **2**. [Available online at <http://www.ejssm.org/ojs/index.php/ejssm/article/viewArticle/32/34>.]
- Trapp, R. J., 2000: A clarification of vortex breakdown and tornadogenesis. *Mon. Wea. Rev.*, **128**, 888–895.
- , and B. H. Fiedler, 1995: Tornado-like vortexgenesis in a simplified numerical model. *J. Atmos. Sci.*, **52**, 3757–3778.
- , and C. A. Doswell, 2000: Radar data objective analysis. *J. Atmos. Oceanic Technol.*, **17**, 105–120.
- Wakimoto, R. M., and C. Liu, 1998: The Garden City, Kansas, storm during VORTEX 95. Part II: The wall cloud and tornado. *Mon. Wea. Rev.*, **126**, 393–408.
- Ward, N. B., 1972: The exploration of certain features of tornado dynamics using a laboratory model. *J. Atmos. Sci.*, **29**, 1149–1204.
- Wicker, L. J., 1996: The role of near surface wind shear on low-level mesocyclone generation and tornadoes. Preprints, *18th Conf. on Severe Local Storms*, San Francisco, CA, Amer. Meteor. Soc., 115–119.
- , and R. B. Wilhelmson, 1995: Simulation and analysis of tornado development and decay within a three dimensional supercell thunderstorm. *J. Atmos. Sci.*, **52**, 2675–2703.
- Wurman, J., 2002: The multiple-vortex structure of a tornado. *Wea. Forecasting*, **17**, 473–504.
- , and S. Gill, 2000: Finescale radar observations of the Dimmitt, Texas (2 June 1995), tornado. *Mon. Wea. Rev.*, **128**, 2135–2164.
- , and M. Randall, 2001: An inexpensive, mobile, rapid-scan radar. Preprints, *30th Int. Conf. on Radar Meteorology*, Munich, Germany, Amer. Meteor. Soc., P3.4. [Available online at <http://ams.confex.com/ams/pdfpapers/21577.pdf>.]
- , and C. Alexander, 2004: Scales of motion in tornadoes. What radars cannot see. What scale circulation is a tornado. Preprints, *22nd Conf. on Severe Local Storms*, Hyannis, MA, Amer. Meteor. Soc., P11.6. [Available online at <http://ams.confex.com/ams/pdfpapers/82353.pdf>.]
- , and —, 2005: The 30 May 1998 Spencer, South Dakota, storm. Part II: Comparison of observed damage and radar derived winds in the tornadoes. *Mon. Wea. Rev.*, **133**, 97–119.
- , J. Straka, and E. Rasmussen, 1996: Preliminary radar observations of the structure of tornadoes. Preprints, *18th Conf. on Severe Local Storms*, San Francisco, CA, Amer. Meteor. Soc., 17–22.
- , J. M. Straka, E. N. Rasmussen, M. Randall, and A. Zahrai, 1997: Design and deployment of a portable, pencil-beam, pulsed, 3-cm Doppler radar. *J. Atmos. Oceanic Technol.*, **14**, 1502–1512.
- , Y. Richardson, C. Alexander, S. Weygandt, and P. F. Zhang, 2007a: Dual-Doppler and single-Doppler analysis of a tornadic storm undergoing mergers and repeated tornadogenesis. *Mon. Wea. Rev.*, **135**, 736–758.
- , —, —, —, and —, 2007b: Dual-Doppler analysis of winds and vorticity budget terms near a tornado. *Mon. Wea. Rev.*, **135**, 2392–2405.
- , C. Alexander, P. Robinson, and Y. Richardson, 2007c: Low-level winds in tornadoes and potential catastrophic tornado impacts in urban areas. *Bull. Amer. Meteor. Soc.*, **88**, 31–46.